Design and Optimization of Micropumps Using Electrorheological and Magnetorheological Fluids

by

Youzhi Liang

Submitted to the Department of Mechanical Engineering
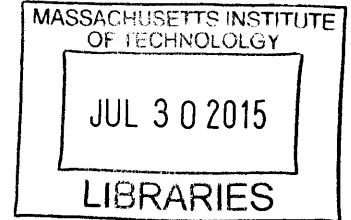in partial fulfillment of the requirements for the degree of

Master of Science in Mechanical Engineering

at the

MASSACHUSETTS INSTITUTE OF TECHNOLOGY

June 2015

Signature redacted

Author . . . .
Department of Mechanical Engineering
May 18, 2015

Signature redacted

Certified by . . . .
Karl Iagnemma
Principal Research Scientist
Thesis Supervisor

Signature redacted

Accepted by . . . .
David E. Hardt
Chairman, Department Committee on Graduate Theses

MITLibraries

DISCLAIMER NOTICE

Due to the condition of the original material, there are unavoidable flaws in this reproduction. We have made every effort possible to provide you with the best copy available.

Thank you.

The images contained in this document are of the best quality available.

Design and Optimization of Micropumps Using Electrorheological and Magnetorheological Fluids

by

Youzhi Liang

Submitted to the Department of Mechanical Engineering
on May 18, 2015, in partial fulfillment of the
requirements for the degree of
Master of Science in Mechanical Engineering

Abstract

Micropumps have rapidly expanded microhydraulic systems into a wider range of applications, such as drug delivery, chemical analysis and biological sensing. Empirical research has shown that micropumps suffer most from their extremely low efficiency.

To improve the efficiency of micropumps, we propose to employ electrorheological (ER) and magnetorheological (MR) fluids as the hydraulic fluids. This thesis presents two methods: one is a dynamic sealing method to be applied on current micro-scale gear pumps using MR fluids, and the other is a novel design method of micropumps using ER fluids.

Using MR fluid with applied magnetic field as a substitute for industrial hydraulic fluids, magnetic chains are aligned within the channel. The parameters, such as magnetic field, viscosity and volume fraction of MR fluid can be balanced to provide optimal sealing performance. Darcy flow through porous media and Bingham flow in a curved channel with a rectangular cross section have been used to model the MR fluid flow exposed to certain magnetic field intensity. Static and dynamic magnetic sealing performance is investigated theoretically and experimentally, which is evaluated by Mason numbers and friction factor.

To achieve a higher efficiency and faster dynamic response, a novel design for micropumps driven by ER fluid is demonstrated. Moving mechanical parts are eliminated by applying a periodic voltage gradient. The approach involves exerting electric forces on particles distributed within the fluid and exploiting drag or entrainment forces to drive flow. Variables are explored, such as the dimension and layout of the channel and electrodes. Experiments are also designed to observe the performance of the solid state pump. In addition, a method of characterizing the efficiency of chamber pump is introduced and applied on screw-chamber pump and solenoid-chamber pump with check valve and ER valve.

Thesis Supervisor: Karl Iagnemma
Title: Principal Research Scientist

3

Acknowledgements

Contents

List of Figures

10

List of Tables

Chapter 1

Introduction

1.1   Micropumps

Micropumps are defined as miniaturized pumping devices by micromachining technologies from the perspective of MEMS [1, 2]. The earliest reported concept of a micropump can be dated back to 1975, mainly consisting of a variable volume chamber, piezoelectric benders and solenoid valve for implantation into human body [2]. After this pioneering work, the concept was oriented towards the MEMS field around 1990 [3]. In recent years, the potential target applications have been widely expanded due to novel physical principles and fabrication methods. Micropumps are commonly used in chemical analyses, biological sensing, and drug delivery [4-6].

Micropumps can generally be classified into two categories: mechanical pumps and non-mechanical pumps. In terms of actuation principles, the most common mechanical methods include piezoelectric [6-8], bimetallic [1], thermopneumatic [9-11], electrostatic [3], electromagnetic actuation [3] and shape memory alloy (SMA) [12-14]; the most common non-mechanical methods include magneto-hydrodynamic (MHD), electro-hydrodynamic (EHD), and electro-osmotic actuation. The most widely used microactuation techniques are summarized in the following with advantages and disadvantaged discussed.

Piezoelectric actuation has been dominant in reciprocating micropumps [2].

This actuation concept is based on the piezoelectric effect which correlates mechanical deformation and electrical polarization [1]. Due to the fast response and precise dosage, piezoelectric micropumps are commonly used to maintain therapeutic efficacy, such as drug delivery [4, 5]. However, the drawbacks for the piezoelectric micropumps are considered to be the high actuation voltage and the mounting procedure [3].

Thermopneumatic micropumps are designed by a periodic change in the volume of the chamber expanded and compressed by a pair of heater and cooler [1]. Micromachining, either for the heater and cooler or the diaphragm, contributes to the realization of this principle [9-11]. The crucial disadvantages for thermopneumatic micropumps is the long thermal relaxation time constant of the cooling process which will limit the bandwidth of the actuation [3], and the driving power which is required to be maintained at a specified-constant level [1].

The shape memory alloy (SMA) micropumps generally refer to those applying the shape memory effect (SME) of SMA among which Titanium/Nickel (TiNi) are most commonly used as being capable of high actuation forces and high recoverable strains, resulting in large pumping rates and high operating pressures [12-14]. The main disadvantages are the relatively high power consumption indicating a low efficiency and the uncontrollable deformation of SMA due to its temperature sensitivity [1].

Considering the efficiency of microhydraulic systems, all types of pumps introduced above suffer from a low efficiency. Typically, the overall efficiency of a micropump is determined by the product of four components: volumetric efficiency, hydraulic efficiency, mechanical efficiency and electrical efficiency. Volumetric losses and hydraulic losses dominate at small scales, although an acceptable efficiency for macropumps has already been achieved. As the size of the system decreases, the volumetric efficiency is dramatically affected since the same

17

dimensional and geometric tolerance result in a larger dimension fraction. In terms of hydraulic efficiency, Reynolds number also decreases as the characteristic length scales decreases, leading to larger viscous losses.
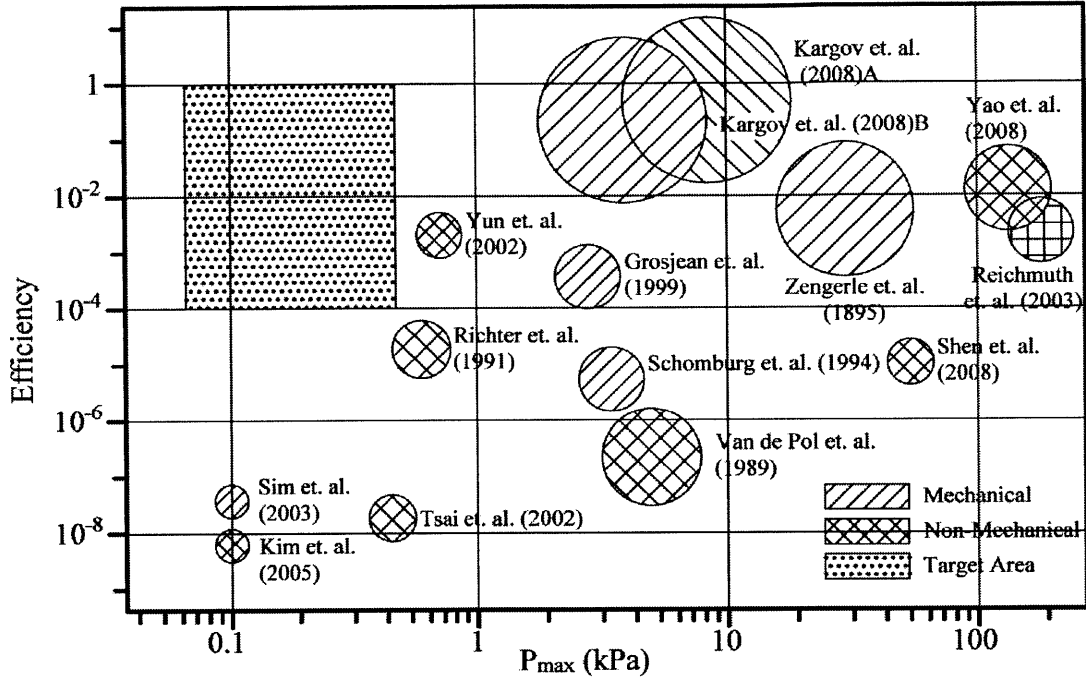
Figure 1-1: Review of efficiency versus maximum pressure for existing small-scale pumping strategies. The different shades denote mechanical or non-mechanical pumps. The size of the symbol depicts the characteristic length scale of the pump package. For reference, Sim $et.$ $al.$ is 72 mm^3 and Kargov $et.$ $al.$ is 18.5 cm^3. The type of each pump is specified as the following: Sim $et.$ al: Micropump with flap valves [15], Kim $et.$ al: Electromagnetic pump [16], Yun $et.$ al: Surface-tension driven pump [17], Richter $et.$ al: Electrohydrodynamic pump [18], Tsai $et.$ al: Thermal-bubble-actuated pump [19], Kargov $et.$ al: Gear pump [20], Grosjean $et.$ al: Thermopneumatic pump [21], Schomburg $et.$ al: Pneumatic chamber pump [22], Van de Pol $et.$ al: Thermopneumatic pump [23], Zengerle $et.$ al: Electrostatic pump [24], Shen $et.$ al: Electromagnetic pump [25], Yao $et.$ al: Electroosmotic pump [26], Reichmuth $et.$ al: electrokinetic pump [27].

18

The efficiencies of reported available micropump technology are shown in Fig. 1-1. The efficiencies of all of most micropumps are less than 1 percent. Especially at low pressure, the efficiency is quite low. The rectangular area indicates the target area of the design of our micro-pumps. Our goal is to build micropumps at low flow rate with a higher efficiency.

1.2 Electrorheological (ER) and magnetorheological (MR) fluids

Electrorheological (ER) fluids and magnetorheological (MR) fluids are both non-colloidal fluids suspended with polarizable particles. These two fluids are capable of being transformed from the liquid state to solid state in milliseconds when exposed in electric or magnetic field [28].

Electrorheological (ER) fluids basically consist of suspended non-conducting particles, up to 100 micrometers, in an insulating fluid [29]. There has been extensive study on the mechanism of ER fluid. Water bridging and polarization of the particles are proposed to explain the shear strength of ER fluids when an electric field is applied [28, 29]. The operational mode for ER fluid can be categorized as flow mode, shear mode and squeeze mode [28]. Typical applications for ER fluids are valves [30-32], clutches [33, 34], absorbers [35, 36], and engine mounts [37, 38].

The wide range of applications benefits from the striking features of ER fluids, like fast dynamic response [32, 41, 42], facile mechanical interface connection [43, 44] and accurate controllability [41, 42]. The response time for DC and AC excitation is on the order of milliseconds, and varies exponentially with the density of the particle [28, 45]. The simplicity of the mechanical structure of the interface connection can be seen in the devices in vales and engine mounts [30-32, 37, 38].

Magnetorheological (MR) fluids are less well known compared to

19

electrorheological (ER) fluids [46]. It is initially used by Jacob Rabinow for a design of clutch in the late 1940s [47]. A commercial success has just been achieved in the recent years [46].

The typical operational mode for the application of MR fluids are pressure driven flow mode and direct shear mode [48, 49]. The most common application is damper, for its appealing features such as low-power consumption, force controllability and rapid response [51]. Especially, the damper for vehicles has been widely investigated and revealed attractive properties [52-54].

The other typical use of MR fluids is the development of MR valves. Compared with ER valves, the most evident advantage is that the apparent viscosity could be controlled by a wider applied magnetic field [55]. In addition, a high efficiency and miniaturization of MR valve have been achieved [56, 57]

Previous research primarily focuses on MR and ER fluids within the scope of high shear stress resulting in large pressure differential or large exerted force [50-57]. However, in this thesis, the low shear stress behavior and dynamic response of ER fluids are mainly studied and applied to the micropump design and micropump sealing.

1.3 Goals

Our goal is to address the inefficiency of micropumps. We propose to employ electrorheological (ER) and magnetorheological (MR) fluids as the hydraulic fluids. In this thesis, MR fluid is investigated for dynamic sealing to be applied on current micro-scale gear pumps; ER fluid is designed to be the hydraulic fluid for a novel design of solid state pump. The theoretical and experimental results to evaluate the performance of dynamic sealing and solid state pump are also presented.

In Chapter 2, four mathematic models for fluids in a curved channel with rectangular cross section are built first, followed by the experimental results of static performance and dynamic performance. A group of dimensionless quantities are defined for the evaluation at last. Chapter 3 includes two sections. The first section discusses the characterization of the performance of chamber pumps. Two kinds of chamber pumps, screw-chamber pump and solenoid pump, are designed and evaluated by a method to characterize the efficiency. The second section elaborates the design of the structure and fabrication of solid state pumps. Experiments are also conducted to observe the performance. Finally, conclusions and future work are briefly summarized in Chapter 4.

Chapter 2

Optimization of Pumps Driven by Magnetorheological Fluid

2.1 Background

Sealing is necessary for micropumps due to its inefficiency discussed in Chapter 1.1. The traditional sealing method for gear pumps is achieved mechanically by controlling the geometric and dimensional tolerance.

This chapter introduces a novel sealing method, applying magnetorheological (MR) fluid as the hydraulic fluid. Simplified mathematical models for a curved channel with rectangular cross section are discussed first, followed by the experimental results and evaluation of the hydraulic performance.

2.2 Magnetorheological Sealing Experiment Design

2.2.1 Mechanical structure

An experimental setup was designed to test the sealing performance with magnetic rheological fluid in terms of the effectiveness of magnetic brush deformation induced by Poiseuille flow and Couette flow. Sealing performance was observed

under the condition of different flow rates and rotational speed of the wall.
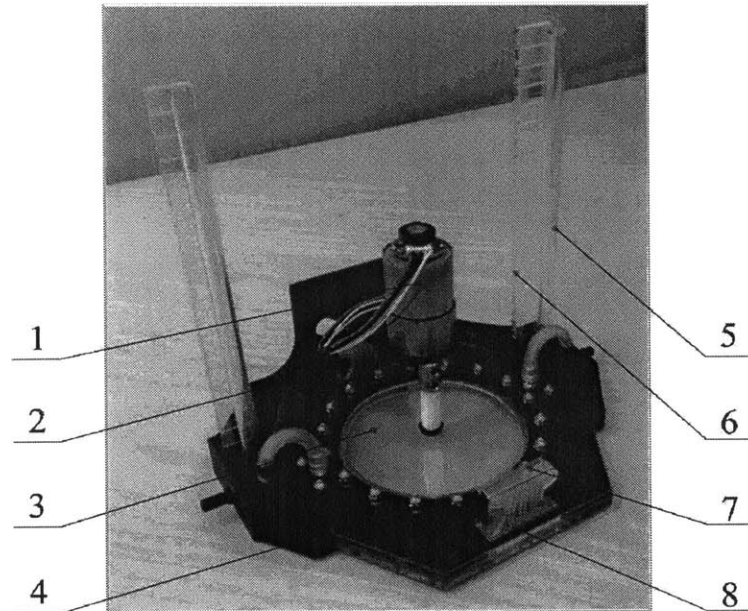
Figure 2-1: A picture of experimental setup. 1: Motor, 2: Frame, 3: Disk, 4: Channel, 5: Pitot tube, 6: Scaled plate, 7: Magnet, 8: Spacers.

As shown in Fig. 2-1, the experimental setup mainly consists of frame, motor, disk, pitot tube and magnet. The frame is designed to secure other components; actually, there is a cavity inside of it, which connects tube fitting, the pitot tube and the tube connected with the disk in the middle. We have built a micro-channel network as Fig. 2-2 shows. A laser cut acrylic sheet was sandwiched between two transparent plates with slots to locate magnets. Spacers are designed to modulate the magnetic field intensity in either channel.

MR fluid flows along the path as the arrow denotes in Fig. 2-2. By exerting magnetic field, magnetic brushes are formed along the channel so that pressure can be hold back. Flow bifurcates into two channels: one channel is exposed to higher magnetic field intensity, which will be treated as a porous media, resulting in a higher fluid resistance; the other one is modeled as Bingham flow due to a lower magnetic field intensity.

To mimic the flow in the gap of gear pumps, one magnet was designed so that stronger magnetic field density could be exerted on the channel where the direction of the flow caused by pressure differential was reverse to that of the Couette flow. Spacers were used to adjust the magnetic field intensity inside of the channels.
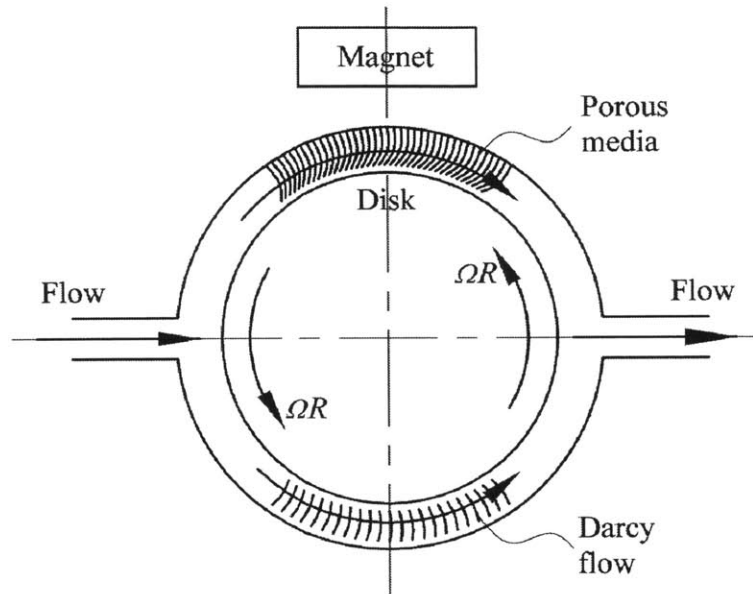
Figure 2-2: A schematic of flow formation. The flow bifurcates into two branches exposed to different magnetic field intensity. A Couette flow rate is also induced by a rotating disk.

The carrier fluid of the MR fluid is Gelest silicone oil 100cSt. MR fluid accounts for 10 percent in volume fraction. The magnets are designed to be quite strong, with a surface field of 1895 Gauss (NdFeB, Grade N42, 2.44 oz.).

Flow rate was controlled by high pressure syringe pumps, ranging from 0.1 mL/min to 0.8 mL/min. The rotational speed of the wheel is set by a DC motor (Pololu 12V) with a variable-voltage power supply and measured via an encoder on the motor.

Pressure at the inlet and outlet of the setup was designed to be measured by both pressure sensors and pitot tubes. Pitot tubes were primarily used to calibrate the

sensors, since the pitot tube was subject to the dynamic response of the fluid, indicating a longer period of time to get stabilized (In the experiment, it took 90 minutes to calibrate sensors).

Experiments were conducted under the condition of flow rates from 0 mL/min to 0.8 mL/min with different rotational speed from 0 rps to 1 rps for three iterations. The magnetic sealing performance was observed and evaluated statically and dynamically.

2.2.2 Electrical Connection

Electric network for the experimental setup is shown in Fig. 2-3. A variable-voltage power supply was used to power both the sensors and the motor, using voltage 10.5 V and from 0 V to 40 V respectively. Data acquired from the sensors were sent to Labview via National Instruments I/O. Arduino was employed to acquire speed feedback from the encoder on the motor.

Aluminum foil was designed to isolate pressure sensors to screen the signal noise from the motor, the power supply and also the strong magnets. The aluminum foil was also grounded with the minus for the sensors and the motor together.
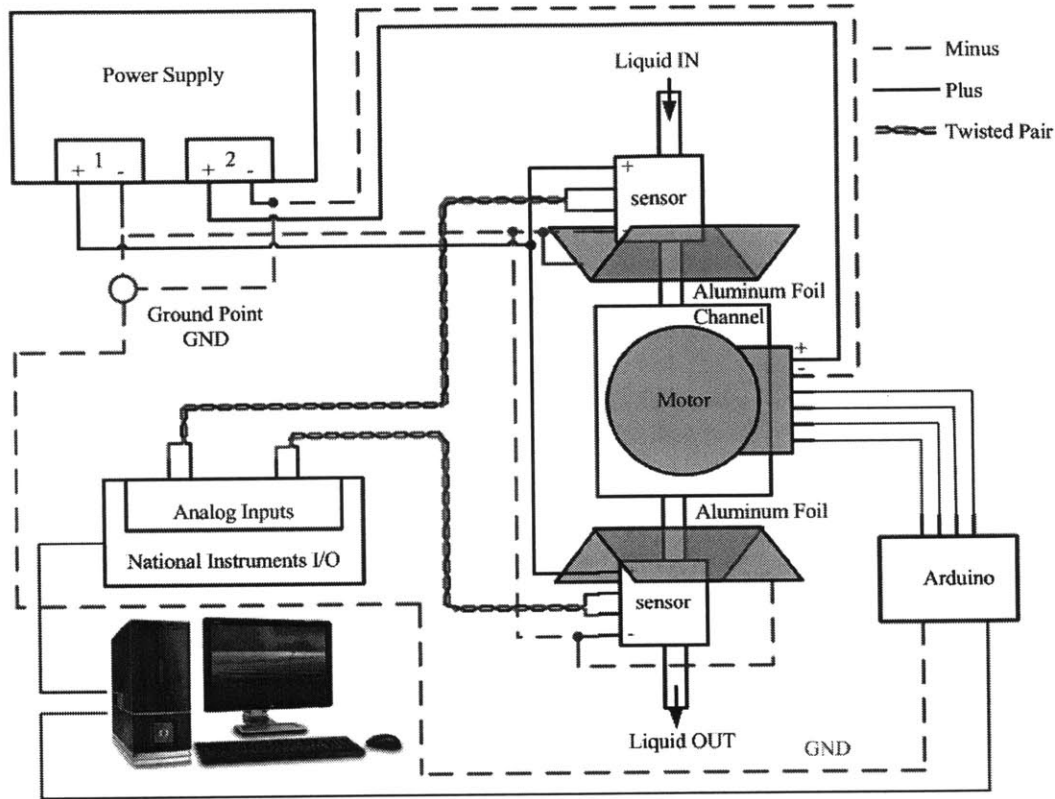
Figure 2-3: A schematic illustration of the electric network of the experimental setup.

2.2.3 Magnetic Field

Shear stress of the MR fluid in presence of magnetic field was determined by the intensity of it besides the volume fraction of the MR fluid in our experiments. The magnetic field intensity was measured by Gauss meter along the circular channel, as shown in Fig. 2-4. For a dipole, theoretically, the intensity decreases by the radius to the third power in Equation (2.1), which indicates the distance between the dipole and the location being measured.

$$B(m, r, \lambda) = \frac{\mu_0}{4\pi} \frac{m}{r^3} \sqrt{1 + 3\sin^2 \lambda} , \qquad (2.1)$$

where B is the strength of the field, r is the distance from the center, λ is the magnetic latitude, m is the dipole moment, μ_0 is the permeability of free space.

Our measurement results show that the magnetic field intensity drops abruptly, and then keeps almost constant. The two (red) planes in Fig. 2-4 denotes the average intensity for the right half circle and the left half one respectively, indicating that the branch immediate to the magnet is 3.8 times larger than that on the further end. Taking the magnetic field direction into account, the intensity within the right further half circle will decrease to 50 % because of a field direction normal to the channel for a large part. This magnetic field intensity distribution lays the foundation for the different mathematical models of the two channels.
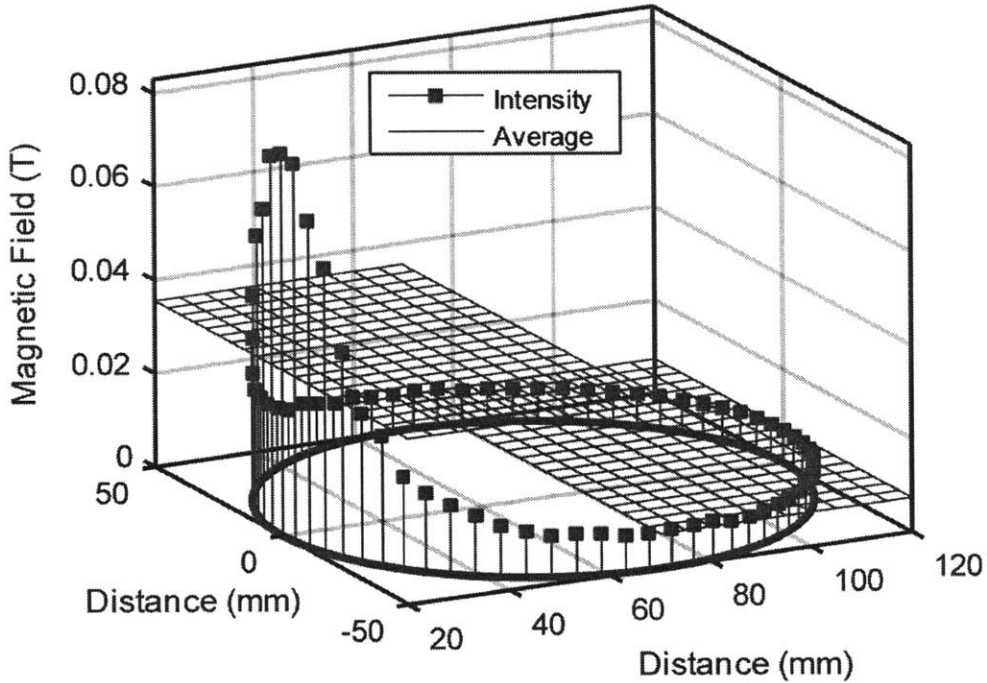
Figure 2-4: Magnetic field intensity distribution along the circular channel. The magnet is 70 mm away from the circular channel with a diameter of 100 mm.

2.3 Models for Flow in Curved Channels with a Rectangular Cross Section

2.3.1 Couette Flow in Curved Rectangular Cross Section Channels

We consider two concentric rotating cylinders with angular speed of Ω_1 and Ω_2 respectively, which are limited by two parallel plates with height h, as Fig. 2-5 shows. This structure forms a rectangular cross-section curved channel. Along the channel, there is no pressure gradient. We employ cylindrical coordinates (r,φ,z), with the z-axis coinciding with the axis of the center line of the cylinders. By applying Navier-Stokes equation, the only non-zero component of velocity is the angular velocity $u_\varphi(r,z)$. This velocity distribution automatically satisfies the continuity equation. The angular equation of motion reduces to

$$0=\mu\left\{\frac{\partial}{\partial r}\left[\frac{1}{r}\frac{\partial}{\partial r}\left(ru_\varphi\left(r,z\right)\right)\right]+\frac{\partial^2 u_\varphi\left(r,z\right)}{\partial z^2}\right\}. \tag{2.2}$$

Non-slip condition:

$$u_\varphi\left(R_1\right)=\Omega_1 R_1,\ \ u_\varphi\left(R_2\right)=\Omega_2 R_2,\ \ u_\varphi\left(z=h/2\right)=0,\ \ u_\varphi\left(z=-h/2\right)=0. \tag{2.3}$$

29
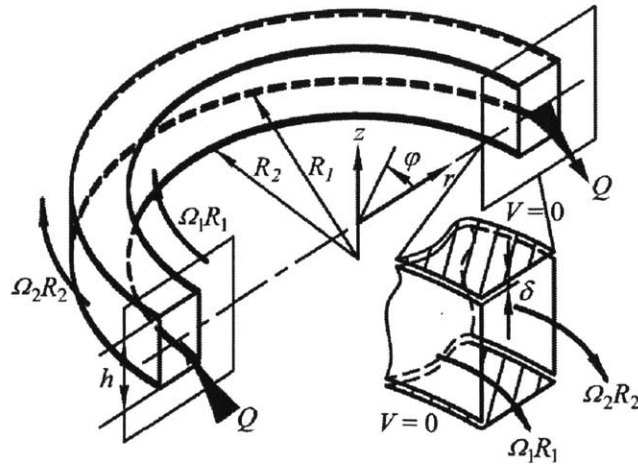
Figure 2-5: A schematic illustration of the flow in a form of Couette flow in a circular channel with rectangular cross section.

(a) Steady Flow between Concentric Rotating Infinite Cylinders

A schematic illustration of the steady flow between concentric rotating infinite cylinders is shown in Fig. 2-6.

Figure 2-6: A schematic illustration of the circular Couette flow. The viscous fluid flows in the gap between an inner cylinder with radius R_1 that rotates at angular speed Ω_1 and an outer cylinder with radius R_2 that rotates at angular speed Ω_2.

Using cylindrical coordinates and assuming that $u = (0, u_\varphi(r), 0)$, the continuity equation is automatically satisfied, and the momentum equations for the radial and tangential directions are the following:

$$-\frac{u_\varphi(r)^2}{r} = -\frac{1}{\rho}\frac{dp}{dr}, \qquad (2.4)$$

$$0 = \eta\frac{d}{dr}\left[\frac{1}{r}\frac{1}{dr}\left(ru_\varphi(r)\right)\right], \qquad (2.5)$$

where ρ is the density of the fluid (units: kg m^{-3}), η is the viscosity (units: Pa s).
Initial conditions:

$$u_\varphi(R_1) = \Omega_1 R_1, \ \ u_\varphi(R_2) = \Omega_2 R_2. \qquad (2.6)$$

Substitution of Equation (2.6) into Equation (2.5) produces the velocity distribution:

$$u_\varphi(r) = \frac{1}{R_2^2 - R_1^2}\left\{ \left[\Omega_2 R_2^2 - \Omega_1 R_1^2\right]r - \left[\Omega_2 - \Omega_1\right]\frac{R_1^2 R_2^2}{r} \right\} \qquad (2.7)$$

When the outer cylinder is static, Equation (2.6) reduce to

$$u_\varphi(r) = \frac{\Omega_1 R_1^2}{R_2^2 - R_1^2}\left(-r + \frac{R_2^2}{r}\right). \qquad (2.8)$$

Substituting $u_\varphi(r)$ into Equation (2.4) give us the pressure distribution, assuming the initial condition is the atmosphere:

$$P_r - P_{R_1} = \frac{\rho \Omega_1^2 R_1^4}{2\left(R_2^2 - R_1^2\right)^2}\left(r^2 - \frac{R_2^4}{r^2} - 4R_2^2 \ln\frac{r}{R_1} - R_1^2 + \frac{R_2^4}{R_1^2} \right) \qquad (2.9)$$

Fig. 2-7 (a) suggests that although $u_\varphi(r)$ derived from the nonlinear Equation (2.8), the velocity distribution within $R_1 = 50$ mm and $R_2 = 52$ mm for our experimental setup shows a nice linearity. The pressure distribution, shown in Fig. 2-7 (b), can be treated as a constant along the channel, since the largest differential of the pressure is less than 5 %. These two distributions are quite similar to the condition for laminar flow in two parallel plates. Therefore, the loss for a concentric rotating cylinder can be simplified as the loss for two parallel plates with the same geometry and dimension.

(a)

(b)
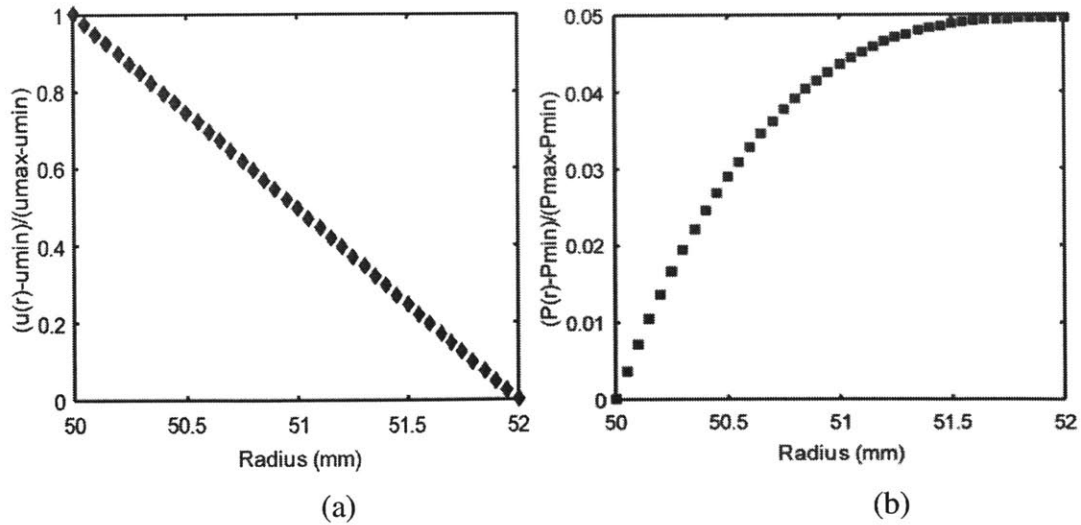
Figure 2-7: Velocity and pressure distribution for concentric rotating cylinder. (a) Velocity distribution. (b) Pressure distribution. Two dimensionless quantities are evaluated by the ratio of the relative value and the span.

(b) Steady Flow between Parallel Plates

The average velocity for Newtonian viscous flow between two parallel plates is $0.5V$, as shown in Fig. 2-8 (a), while limited by another two parallel plates, the average velocity reduces to $0.19V$, as shown in Fig. 2.8 (b).

The boundaries are considered to exert a linear decrease on the initial velocity distribution. A clearance δ, as shown in Fig. 2-5, is necessary to take into account otherwise two singular points at the corner of the moving plate will occur because of an infinite velocity gradient. Given the specific experimental setup as described in Chapter 2.1, velocity distribution within a squared area is calculated to be $0.19V$ as shown in Fig. 2-9.

Therefore, the average velocity of the flow between two concentric rotating cylinders is given by

$$
\begin{aligned}
\overline{u_\varphi} &= \varphi \frac{\displaystyle\int_{R_1}^{R_2} u_\varphi(r)\,r\,dr}{R_2 - R_1} = \varphi \frac{\Omega_1 R_1^2}{(R_2 - R_1)(R_2^2 - R_1^2)} \int_{R_1}^{R_2}\left(-r + \frac{R_2^2}{r}\right) r\,dr \\
&= \varphi \frac{\Omega_1 R_1^2 \left(R_1^3 + 2R_2^3 + 3R_1 R_2^2\right)}{3(R_2 - R_1)(R_2^2 - R_1^2)}
\end{aligned}
\tag{2.10}
$$

where φ is the constant factor $0.19/0.5$.

(a) (b)
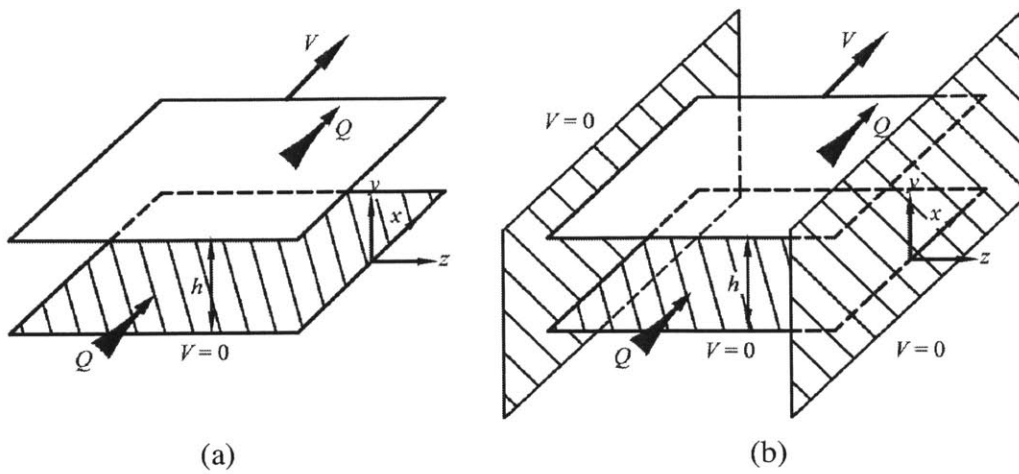
Figure 2-8: Schematics for Couette flow between parallel plates. (a) Couette flow between infinite parallel plates. (b) Couette flow between parallel plates limited by two static parallel boundaries.
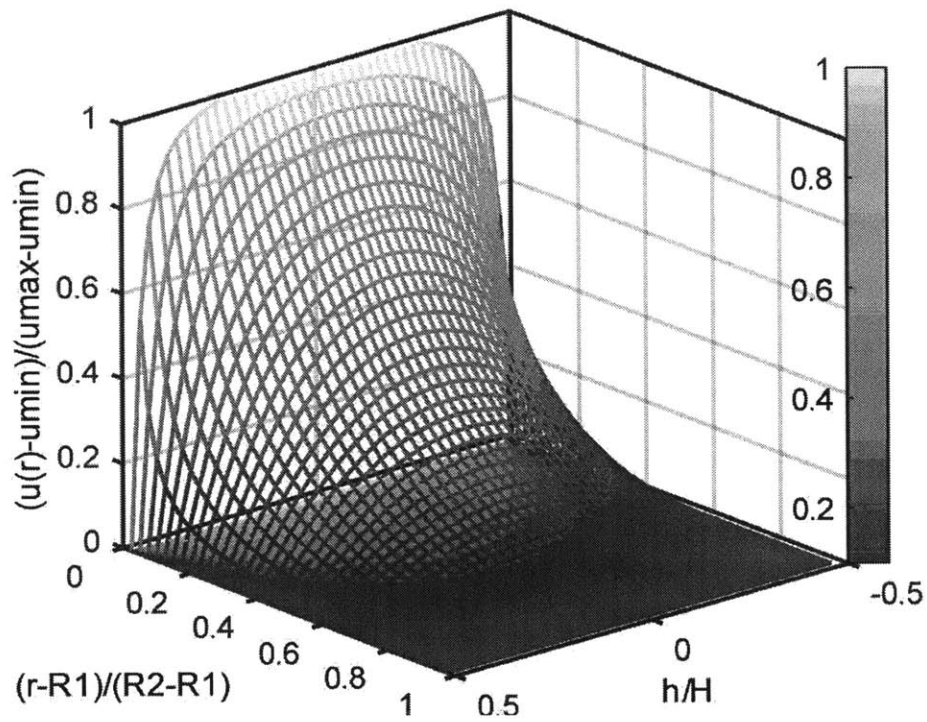
Figure 2-9: Velocity distribution. Dimensionless quantities are evaluated by the fraction.

2.3.2 Poiseuille Flow in Curved Rectangular Cross Section Channels

We attempt to approach the solution in a simpler method to the real velocity distribution of the Poiseuille flow in a curved rectangular cross section channel by diving it into three steps: to solve for the velocity distribution of Poiseuille flow in a channel between two concentric infinite cylinders; to solve for the velocity distribution of the Poiseuille flow in a channel between two parallel infinite plates; to substitute the velocity distribution between cylinders into that between plates as the peak. A schematic illustration of the circular Poiseuille flow is shown in Fig. 2-10.
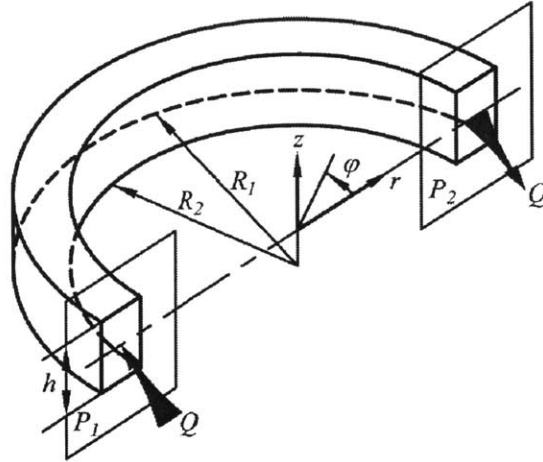
Figure 2-10: A schematic illustration of the circular Poiseuille flow. The viscous fluid flows in the rectangular cross section channel, which is driven by pressure gradient $(P_1 - P_2)/\pi r$.

Assuming that $u = (0, u_\varphi(r), 0)$, the Navier-Stokes equation in the tangential direction written in cylindrical polar coordinates in the absence of body force is

$$0 = \eta \left[\frac{\partial}{\partial r} \left(\frac{1}{r} \frac{\partial}{\partial r} \left(r u_\varphi(r,z) \right) \right) + \frac{\partial^2 u_\varphi(r,z)}{\partial z^2} \right] - \frac{1}{r} \frac{\partial p}{\partial \varphi}, \qquad (2.11)$$

where η is the viscosity of the fluid, $\partial p / \partial \varphi$ is $(P_1 - P_2)/\pi$.

Initial conditions:

$$u_\varphi\left(r=R_1\right)=0, \ u_\varphi\left(r=R_2\right)=0, \ u_\varphi\left(z=h/2\right)=0, \ u_\varphi\left(z=-h/2\right)=0. \tag{2.12}$$

(a) Poiseuille Flow between Concentric Infinite Cylinders

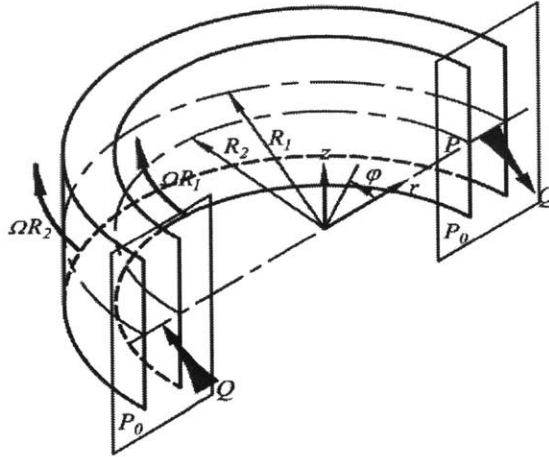A schematic illustration of Poiseuille flow between two concentric infinite cylinders is shown in Fig. 2-11.
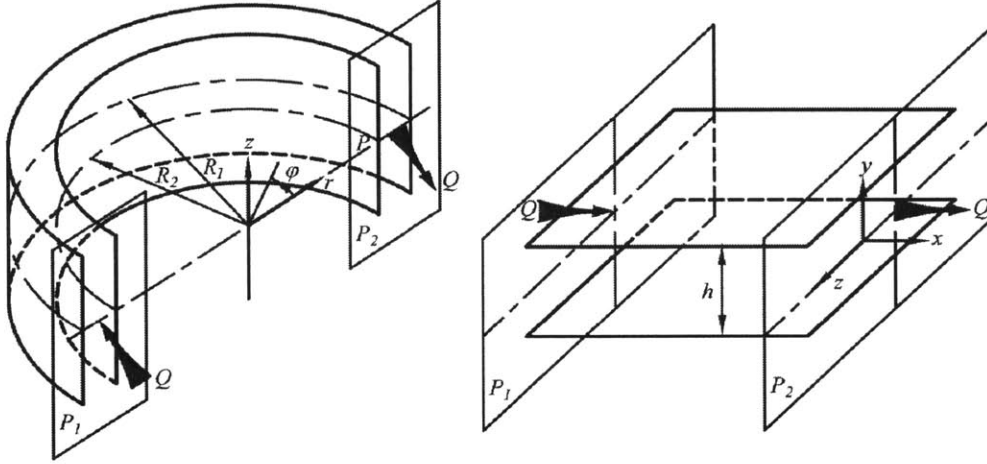
Figure 2-11: Schematics for Poiseuille flow between parallel plates. Flow is driven by pressure gradient from P1 to P2. (a) Poiseuille flow between infinite parallel plates. (b) Poiseuille flow between parallel plates limited by two static parallel boundaries.

Assuming that the tangential velocity u_φ is dependent of r and z, the Navier-Stokes equation reduces to

$$0=\eta\frac{\partial}{\partial r}\left(\frac{1}{r}\frac{\partial}{\partial r}\left(ru_\varphi\left(r,z\right)\right)\right)-\frac{1}{r}\frac{\partial p}{\partial \varphi} \tag{2.13}$$

No slip conditions:

$$u_\varphi\left(r=R_1\right)=0; \ \ u_\varphi\left(r=R_2\right)=0 \tag{2.14}$$

With the initial conditions from Equation (2.14), the partial Equation (2.13) can be solved for the velocity distribution:

$$u_\varphi\left(r\right)=\frac{1}{2\mu}\left(\frac{\partial p}{\partial \varphi}\right)\left[r\ln r-\frac{R_1^2\ln R_1-R_2^2\ln R_2}{R_1^2-R_2^2}r+\frac{R_1^2R_2^2\left(\ln R_1-\ln R_2\right)}{R_1^2-R_2^2}\frac{1}{r}\right] \tag{2.15}$$

(b) Poiseuille Flow between Infinite Parallel Plates

As Fig. 2-11 (b) shows, the Poiseuille flow between two parallel infinite plates driven by pressure differential can be solved with initial conditions:

$$0 = \mu \frac{\partial^2 u_x(y)}{\partial y^2} - \frac{\partial p}{\partial x} \tag{2.16}$$

$$u_\varphi(z = h/2) = 0, u_\varphi(z = -h/2) = 0. \tag{2.17}$$

Velocity distribution is:

$$u_x(y) = \frac{1}{\mu} \frac{\partial p}{\partial x} y^2 - \frac{1}{\mu} \frac{\partial p}{\partial x} \frac{h^2}{4} \tag{2.18}$$

Rewrite Equation (2.18) expressed by the peak:

$$u_x(y) = u_{x\_max}(r) y^2 - u_{x\_max}(r) \frac{h^2}{4} \tag{2.19}$$

We assume that the effect of the two parallel plates is to reduce the velocity to zero at the boundaries in a form of parabola. In addition, the velocity distribution in the r-direction remains a pattern as $u_\varphi(r)$. Given the geometric symmetry in z-direction, the maximum velocity it can reach, if possible in terms of z-direction, must be $u_\varphi(r)$. Therefore,

$$u_{x\_max}(r) = u_\varphi(r) \tag{2.20}$$

Substitute Equation (2.19) into Equation (2.15):

$$u_\varphi(r, y) = \frac{1}{2\mu} \left(\frac{\partial p}{\partial \theta} \right) \left[r \ln r - \frac{R_1^2 \ln R_1 - R_2^2 \ln R_2}{R_1^2 - R_2^2} r + \frac{R_1^2 R_2^2 (\ln R_1 - \ln R_2)}{R_1^2 - R_2^2} \frac{1}{r} \right] \left(y^2 - \frac{h^2}{4} \right) \tag{2.21}$$

The result of the velocity distribution of the Poiseuille flow between two parallel infinite plates is shown in Fig. 2-12.

36
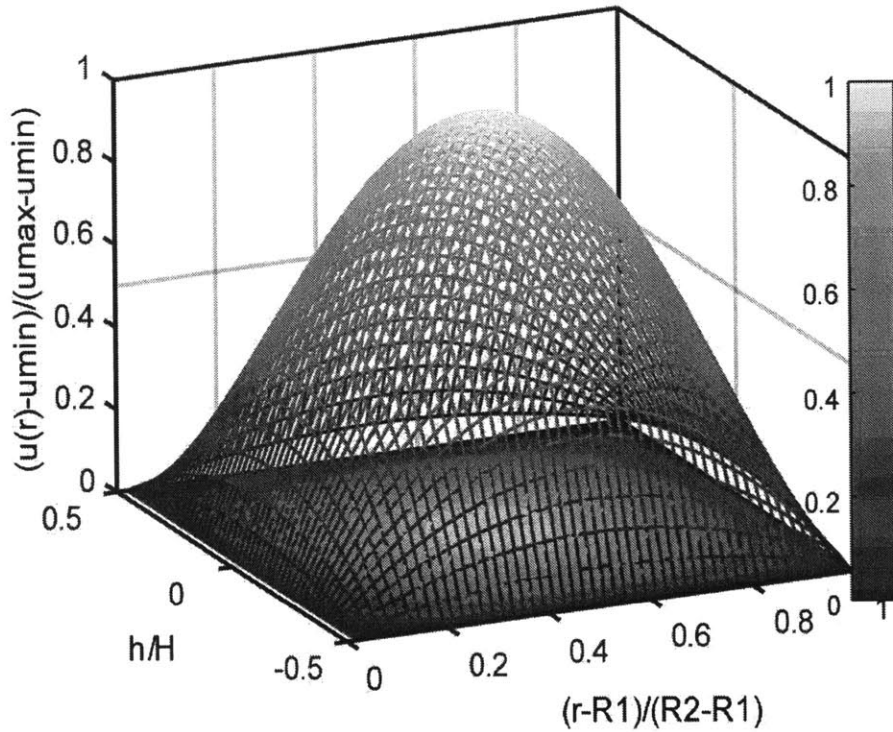
Figure 2-12: Velocity distribution. Dimensionless quantities are evaluated by the fraction.

Using silicone oil with known viscosity 0.0974 Pa·s (Gelest silicone oil 100cSt; Experimental result of the measurement by rheometer is (0.09979 ± 0.00114) Pa·s shown in Table 2-1), we conducted a group of experiments to measure the viscosity of it to verify of the mathematical model introduced above by the experimental setup as shown in Fig. 2-12. Fig. 2-13 indicates a viscosity of 0.115 Pa·s, which agrees with the specification from manufacturer very well.

Table 2-1: Viscosity Measurement for Gelest Silicone Oil 100cSt

Shear Stress (Pa)	Strain Rate (1/s)	Viscosity (Pa·s)
0.9939	9.866	0.1007
1.459	14.30	0.1020
2.141	21.62	0.9905

3.143	31.06	0.1012
4.613	45.50	0.1014
6.771	68.20	0.09928
9.939	100.2	0.09923
14.59	147.1	0.09915
21.41	215.7	0.09926
31.43	315.3	0.09967
46.13	465.7	0.09906
67.71	685.0	0.09984
99.38	1010	0.09938
	Mean	0.09979
	Standard Deviation	0.00114

Figure 2-13: Viscosity measurement. Pressure differential (psi) as a function of flow rates (mL/min). Each point corresponds to the mean from three iterations of experiments, with error bars indicating standard deviation.

2.3.3 Bingham Flow for Magnetorheological Fluid

A conventional model used to characterize MR fluid for simple analysis is the Bingham plastic model, though MR fluid is also known to be subject to shear thinning, and below the yield stress, behaves as a viscoelastic material dependent on magnetic field intensity. A slight tendency of shear thinning was observed in the viscosity measurement of the MR fluid used for experiments, shown in Table 2-2, MR fluid is still considered to be Bingham fluid because a small deviation accounts for the conditions for the experiments in this thesis.

Table 2-2: Viscosity Measurement for MR Fluid

Shear Stress (Pa)	Strain Rate (1/s)	Viscosity (Pa·s)
0.9966	5.569	0.1789
1.463	8.122	0.1801
2.147	11.90	0.1804
3.151	17.50	0.1801
4.626	26.01	0.1779
6.790	37.99	0.1787
9.966	55.03	0.1811
14.63	82.83	0.1766
21.47	121.3	0.1770
99.65	565.9	0.1761
	Mean	0.17835
	Standard Deviation	0.00168

The flow behavior is shown in Fig. 2-14. In region I and III, MR fluid behaves

much like Newtonian fluid. When the shear stress is as large as τ_0, MR fluid flows as a solid in region II.
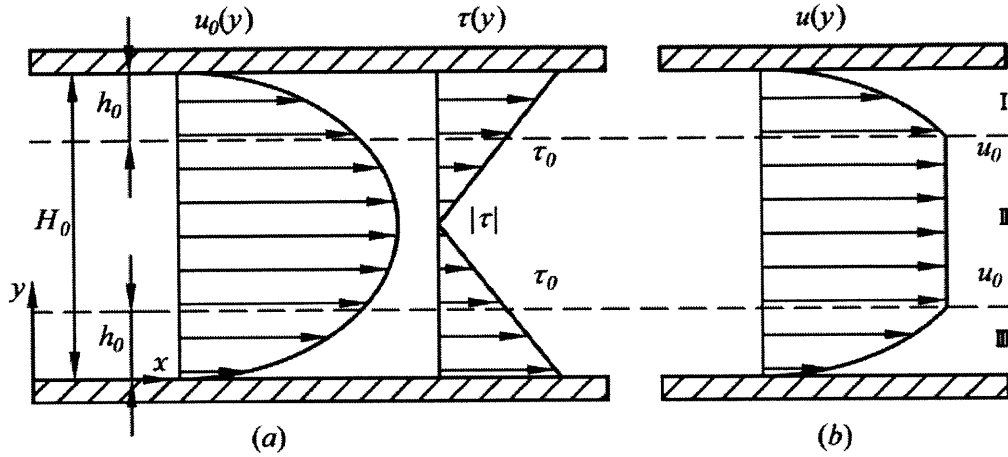
Figure 2-14: A schematic illustration of the Bingham flow model. (a) Newtonian flow through parallel plates. (b) Bingham flow through parallel plates.

The Bingham constitutive relation can be written as

$$\tau = \pm \tau_0 (H) + \eta \frac{du}{dz}, |\tau| > |\tau_0|,$$
(2.21)

where τ_0 is the yield stress, H is the magnetic field, η is the viscosity, and du/dz is the velocity gradient in z-direction.

The velocity distribution for Newtonian flow in Fig. 2-14 (a) is

$$u_0(y) = \frac{1}{2\eta} \left(-\frac{dp}{dx} \right) (H_0 y - y^2),$$
(2.22)

where η is the viscosity of MR fluid unexposed to magnetic field, dp/dx is the pressure gradient.

$$\tau = \eta \frac{du(y)}{dy} = \frac{1}{2} \left(-\frac{dp}{dx} \right) (H_0 - 2y)$$
(2.23)

40

when $\tau = \tau_0$, we have the h_0, within which MR fluid behaves as Newtonian fluid:

$$h_0 = \frac{1}{2}H_0 - \frac{\tau_0}{\left(-\dfrac{dp}{dx}\right)}.$$ (2.24)

Therefore, the velocity distribution $u(y)$ for MR fluid using Bingham model is

$$u(y) = \frac{1}{2\eta}\left(-\frac{dp}{dx}\right)\left(H_0 y - y^2\right), \quad y \in [0,h_0] \cup [H_0 - h_0, H_0];$$ (2.25)

$$u(y) = \frac{1}{2\eta}\left(-\frac{dp}{dx}\right)\left(H_0 y_0 - y_0^2\right), y \in [h_0, H_0 - h_0].$$ (2.26)

The total flow rate through the channel is

$$Q = \int_0^{H_0} u(y)dy = \frac{2}{3\eta}\left(-\frac{dp}{dx}\right)\left(y_0^2 - \frac{3}{2}H_0 y_0 + \frac{3}{4}H_0^2\right)y_0$$ (2.27)

2.3.4 Darcy Flow for Magnetorheological Fluid

MR fluid is typically modeled as Bingham flow. However, when the largest flow rate in the vicinity of the walls of the channel is smaller than τ_0, the fluid will be kept statically inside, acting as a porous media.

Darcy's law can be represented as a simple proportional relationship between the flow rate through a porous medium, the viscosity of the fluid and the pressure drop over a given distance, as Equation (2.28).

$$Q = \frac{-\kappa}{\eta}\left(-\frac{dp}{dx}\right),$$ (2.28)

where η is the viscosity, dp/dx is the pressure gradient along the porous channel, κ [m^2] is the permeability of the medium. For MR fluid, the permeability κ depends on the magnetic field density, the geometry of the channel and the pressure gradient.

41

2.4 Static Performance

Using the experimental setup shown in Fig. 2-1, we conducted experiments with and without magnet. Speed of the disk was set to be zero in both cases. Silicone oil with known viscosity was first tested as a calibration for the setup. The viscosity of MR fluid with magnet is 3.15 times as large as that of silicone oil. Neither of the fitting line crosses the origin, indicating a constant loss of the setup which may be explained by the curved tubing, increasers and reducers, and the constant offset error of sensors.
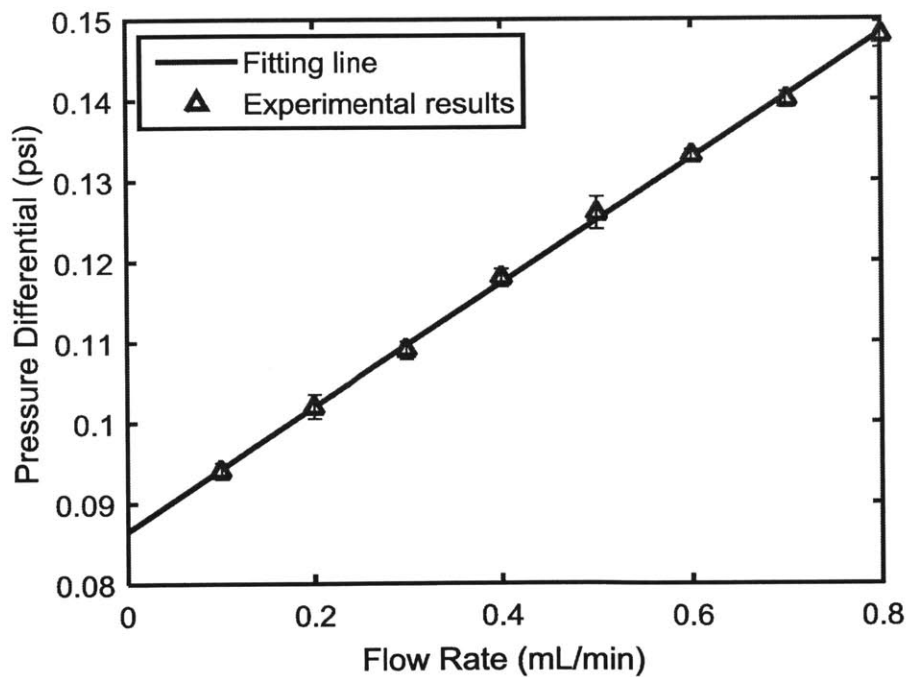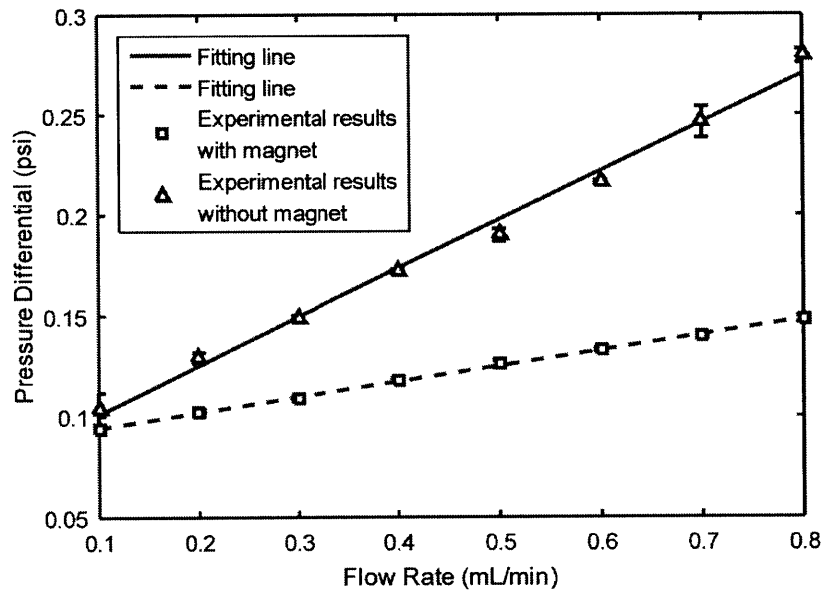

Figure 2-15: Viscosity measurement. Pressure differential (psi) as a function of flow rates (mL/min). Each point corresponds to the mean from three iterations of experiments, with error bars indicating standard deviation. The experiments without magnet was conducted with known viscosity (0.09979 ± 0.00114) Pa·s.

2.4.1 Performance under Poiseuille Flow

Experiments were designed to study the performance with a weak magnetic field (0.008 T). The mathematical model is detailed in Chapter 2.2. We have built a microchannel network made of a silicon slide, which is laser-cut and sandwiched between two acrylic plates. The flow was driven by pressure gradient using a syringe pump to control the flow rate.

(a)　　　　　　　　(b)　　　　　　　　(c)

(d)　　　　　　　　(e)　　　　　　　　(f)
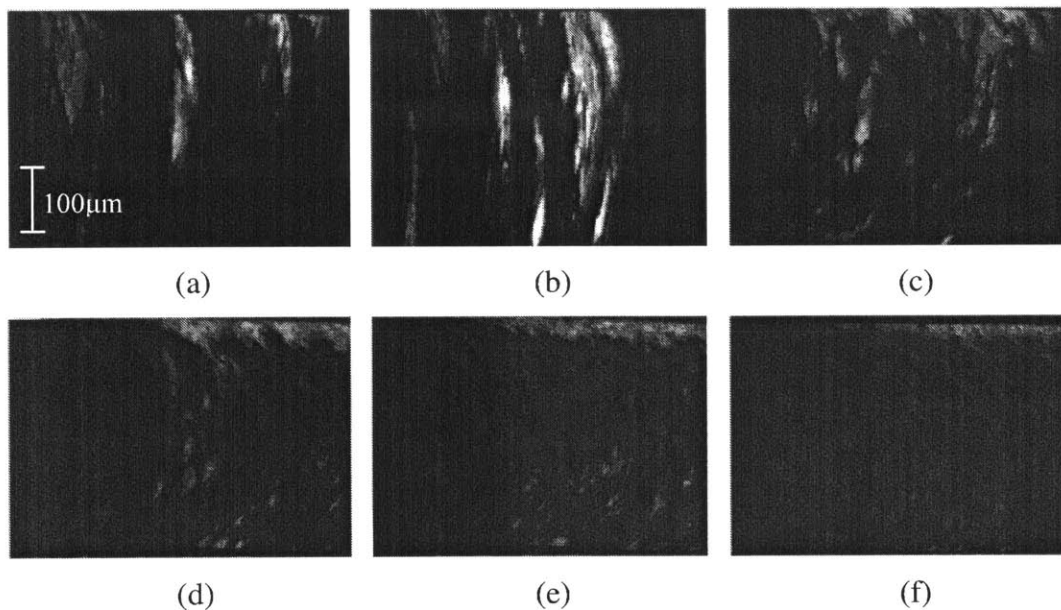
Figure 2-16: Deformation of magnetic chains for different flow rates (Channel width: 0.7 mm, viscosity: 1.78 Pa·s, MR fluid volume fraction: 10%). Flow rates from (a) to (i): 0.01 mL/min, 0.1 mL/min, 1 mL/min, 5 mL/min, 10 mL/min, 15 mL/min.

Typical deformations in the channel for different flow rates are displayed in Fig. 2-16 (c). It suggests that the deformation of the magnetic chains is more evident as flow rates increases and the magnetic chains finally collapse.

Notice that with low flow rate, magnetic chains tend to aggregate in bunches with slight deformation. These chains appear to attach with the vicinity of the walls

of the channel. As the flow rate increases, the chains are more evidently deformed and segregated. It can be observed in Fig. 2-16 (d) that chains start to break at flow rate of 2 mL/min due to higher shear stress, resulting in the detachment from the walls of the channel. After the flow rate at which chains collapse, the channel is filled with uniform particles, the density of which do not change significantly with higher flow rates as shown in Fig. 2-16 (e), (f).

To verify the mathematical model for the magnetic sealing performance at static state, three groups of experiments have been done, and each group of experiments have been repeated for three iterations. Flow rate is controlled by syringe pump, ranging from 0 mL/min to 1.6 mL/min. Pressure differential is acquired by gauge pressure sensors. The experimental results for three different channel widths are shown in Fig. 2-17.
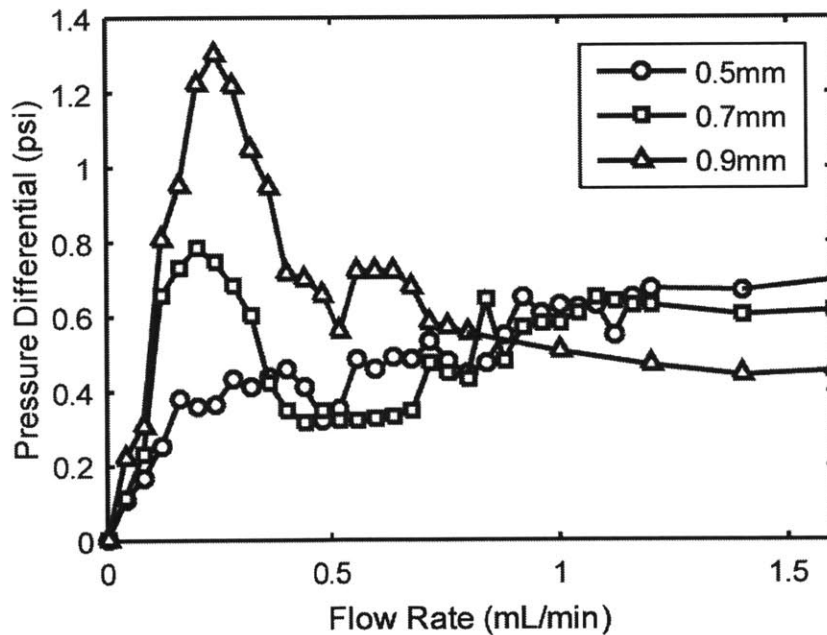
Figure 2-17: Pressure differential (psi) as a function of flow rate (mL/min), for channel widths from 0.5 mm to 0.9 mm. Each point corresponds to the mean from three iterations of experiments.

As shown in Fig. 2-17, there is a clear pattern shows that the pressure differential will grow as flow rate increases from 0 mL/min; after the peak, if any, it decreases and finally reaches a constant value.

The experimental results are striking. First, the peak point gets more obvious as the width of the channel increases. As for the 0.5 mm channel, the peak can hardly be seen, while the peaks are evident to reach almost 0.8 psi and 1.3 psi for 0.7 mm channel and 0.9 mm channel respectively. Also, the peak happens at the flow rate of around 0.2 mL/min. It seems that as the channel width increases the peak point will be pushed backward. Furthermore, the slope at 0 mL/min suggests gets steeper as the channel width increases, indicating that the pressure differential grows faster when the channel width is large.

Second, the data suggest that the final value of the pressure differential decreases as the width of the channel gets larger. It appears that it is a non-linear decrease since the difference of the final value of the pressure differential between 0.5 mm channel and 0.7 mm channel is about 0.1 psi, while that between 0.7 mm channel and 0.9 mm channel is nearly 0.2 psi, almost as twice as the former one.

Third, the data indicate that there is a transition between the flow rate of 0.8 mL/min and that of 1.0 mL/min. The intersections of pressure differential under different flow rates happen within the scope of this range. Before this transition, the pressure differential is higher for wider channel width; after this transition, the result is just the opposite.

It can be noticed that, somewhat surprisingly, the peak point lags behind as the channel width gets larger, while the transition point advances. Therefore, as the channel width gets larger and larger, there can be an overlap flow rate range for these two effects. Presumably, these two effects may counteract with each other and finally this interaction may lead to an offset, indicating a flatter and flatter curve when the channel width is large enough.

2.4.2 Performance under Couette Flow

Another experiment was designed to observe the deformation of magnetic brushes under Couette flow. The moving wall was achieved by a disk driven by a motor, of which the rotational speed ranged from 0 rps to 1 rps.

As shown in Fig. 2-17, the left black area of each figure depicts a roughened stationary surface, and the right one depicts a moving wall. As the rotational speed increases, the density of magnetic brushes dramatically decreases with a larger curvature. In addition, the flow rate induced by the rotational disk is reduced by the magnetic brushes; in return, the brushes break when the shear stress is larger than the yield stress.

(a)	(b)	(c)
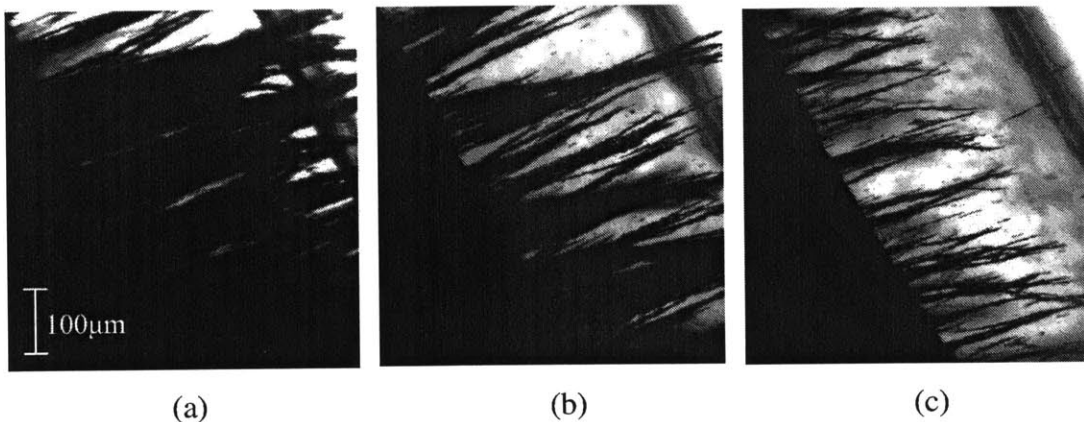
Figure 2-18: Deformation of magnetic chains for rotational speed (Channel width: 0.7 mm, viscosity 0.97 Pa·s, MR fluid volume fraction 1%). Rotational speed from (a) to (c): 0 rps, 0.4 rps, 0.8 rps.

46

2.5 Dynamic Performance

2.5.1 Hydraulic Performance

Experiments were designed to investigate the sealing performance. The experimental setup is elaborated in Chapter 2.2. Assuming a constant equivalent viscosity of the fluid, the pressure differential increased linearly as a function of flow rate. As the rotational speed increased, the pressure differential went down abruptly from the static state to the dynamic due to the unequally induced Couette flow rate resulted from the asymmetric magnetic field intensity. The flow is modeled as Darcy flow through porous media for one branch, and as Bingham flow for the other. The flow rate induced by the rotational speed of the disk was reduced by the porous media in the branch exposed in stronger magnetic field. This asymmetric induced flow rate accounted for the discrepancy of the pressure differential between the static state and the dynamic. However, as the rotational speed increases, the pressure differential remained nearly stable, indicating that the effectiveness of the porous media was restrained, which could be accounted by the excess of the deformation saturation of magnetic brushes.

Figure 2-19: Dynamic sealing performance. Pressure differential (psi) as a function of rotational speed (rps), for flow rates from 0.1 mL/min to 0.8 mL/min. Each point corresponds to the mean from three iterations of experiments, with error bars indicating standard deviation.

2.5.2 Power Dissipation

A group of experiments were designed to check the hydraulic performance in terms of power dissipation. As shown in Fig. 2-20, the experimental results suggest that as the rotational speed increases, the power input required gets larger, which is in agreement with the theory that the Couette flow rate induced increases, resulting in a larger power dissipation.

In the experiments, an obvious hysteresis could be noticed for flow rate larger than 0.5 ml/min, resulting in instability for the condition of larger flow rates and larger rotational speed.

48
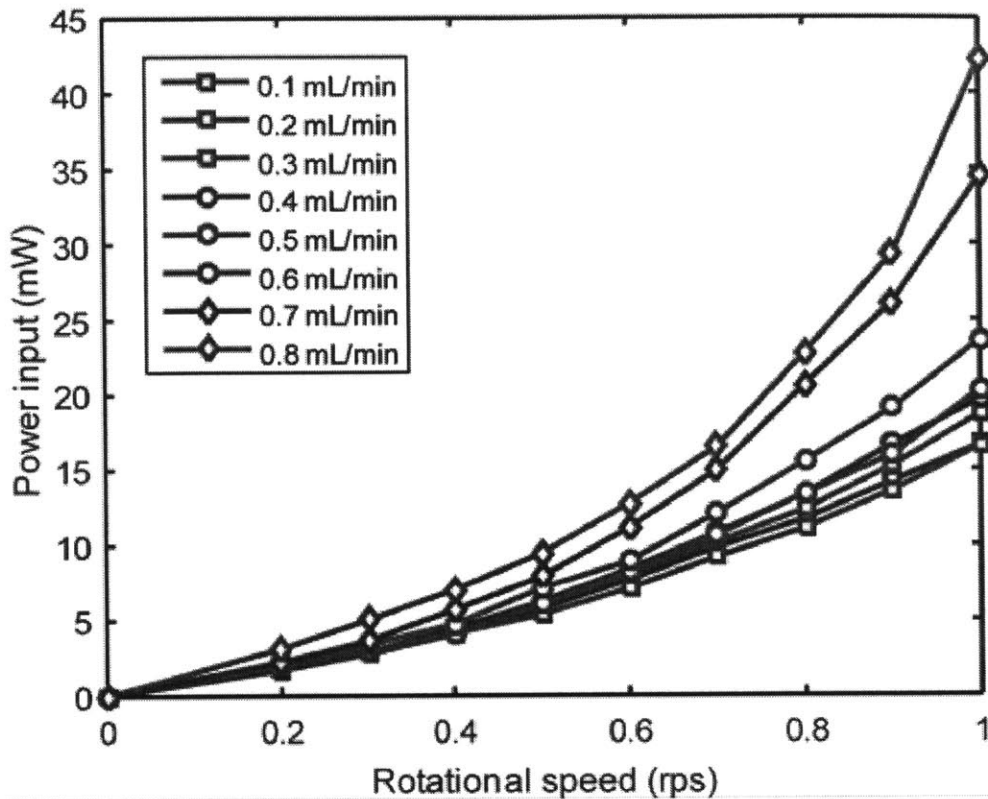
Figure 2-20: Power dissipation. Power input (mW) as a function of rotational speed (rps), for flow rates from 0.1 mL/min to 0.8 mL/min. Each point corresponds to the mean from three iterations of experiments.

2.6 Discussions and Evaluations

2.6.1 Dimensional Analysis

The solution variable in our model is the pressure differential between the inlet and outlet ΔP. The primary variables derives from the geometry, kinematic and the property of the fluid and magnetic field: the diameter of the middle disk D, the width of the channel w, the height of the channel H; viscosity of the fluid with no presence of magnetic field η; the property of the magnetic field B/μ^2 in which B is the magnetic field intensity and μ is the magnetic permeability; the average velocity of

49

the fluid within the channel U and the rotational velocity of the middle disk ω.

By inspection, the dimensionless groups are constructed:

$$\Delta P \frac{\mu}{B^2} \frac{h}{L} = \Phi(\frac{R}{h} \frac{\mu}{B^2} \eta \omega, \frac{w}{D}, \frac{H}{D}, \frac{U}{D\omega}) \qquad (2.29)$$

where $\Delta P \frac{\mu}{B^2} \frac{h}{L}$ is defined as Mason #2, $\frac{R}{h} \frac{\mu}{B^2} \eta \omega$ as Mason #1, $\frac{U}{D\omega}$ as

dimensionless velocity. The definition of friction factor conforms to the convention,

defined as $f = \Delta P / \frac{1}{2} \rho U^2 \frac{L}{D_k}$.

2.6.2 Evaluation by Friction Factor and Mason Number

The hydraulic performance of the magnetic sealing, using experimental setup shown in Fig. 2-1, is evaluated by friction factor and Mason number illustrated in Fig. 2-21 and Fig. 2-22 respectively.

Fig. 2-21 suggests that the friction factor experiences a gradually steady growth and dramatically steep increase as Mason #2 decreases. Friction factor, in our experiments, typically indicates the energy loss within the channel, and the Mason #2 directly reflects the pressure differential used to drive Poiseuille flow. The result of this evaluation conforms to the experimental observation that when the pressure differential is low, the density of the magnetic brushes is high with slight deformation, resulting in a higher energy loss.

Fig. 2-22 basically reflects the correlation of the influence of Poiseuille flow and Couette flow. The pattern for Mason #2 and the dimensionless velocity is striking, which can be simply explained by the rotational speed defined in these two dimensionless groups. On the contrary, Mason #2 decreases slightly as Mason #1 varies, suggesting that the influence of Couette flow does not dominate in our experiments. It is considered that the velocity of the disk will induce the maximum deformation of the magnetic brushes as long as the disk starts to rotate.
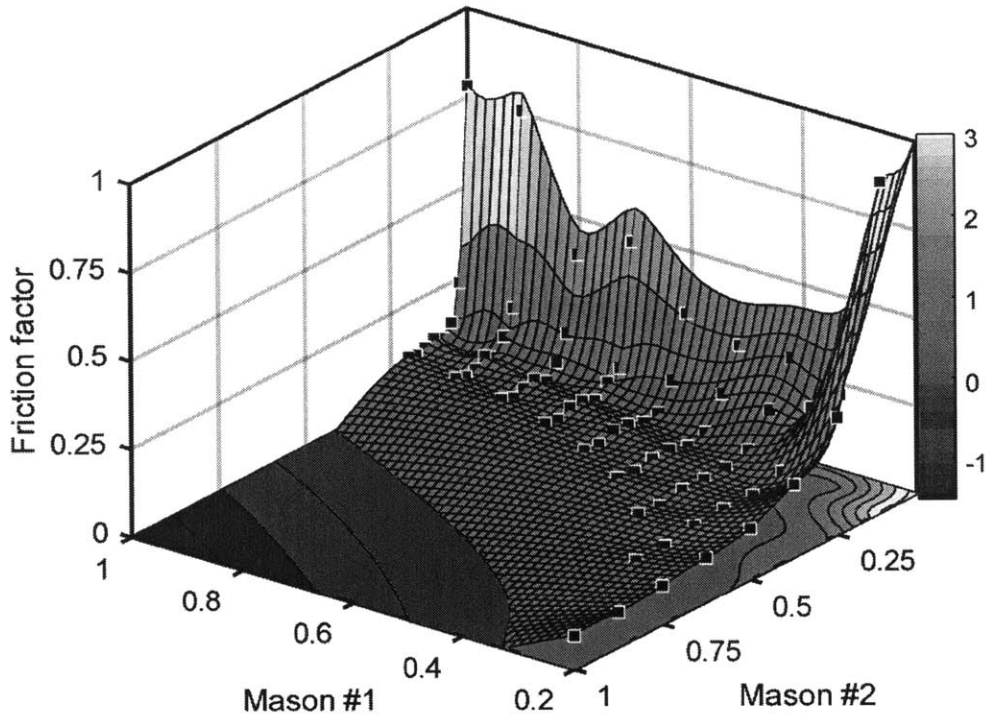
Figure 2-21: Hydraulic performance evaluated by Friction factor. The ranges of the three dimensionless groups in the figure are scaled down from 0 to 1.
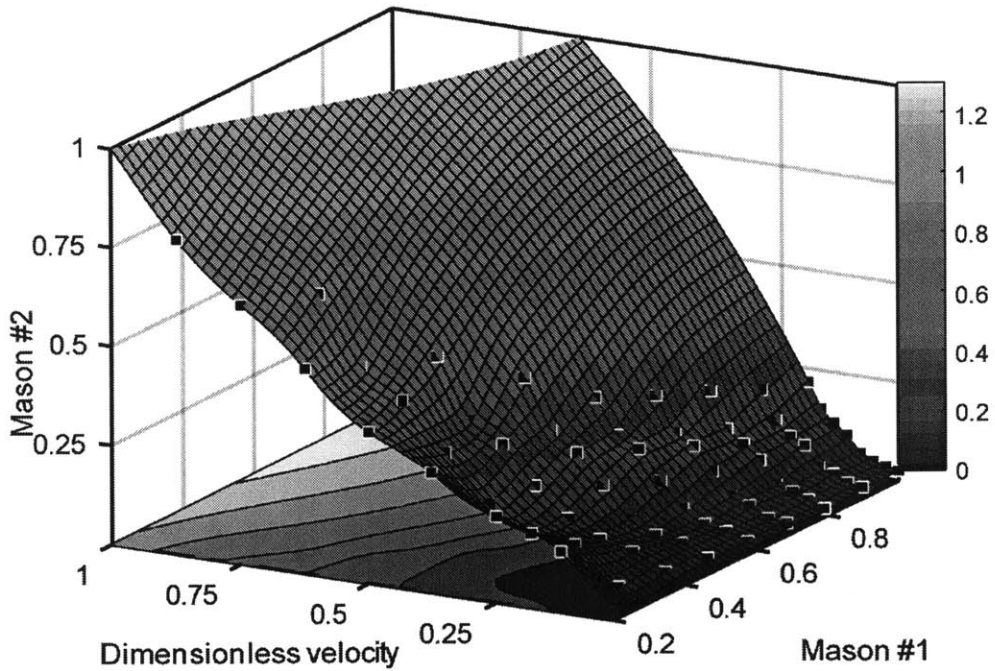
Figure 2-22: Hydraulic performance evaluated by Mason #2. The ranges of the three dimensionless groups in the figure are scaled down from 0 to 1.

Chapter 3

Design of Pumps Driven by Electrorheological Fluid

3.1   Background

Micropumps can generally be classified into two categories: mechanical pumps and non-mechanical pumps. The most common mechanical actuation methods include piezoelectric, bimetallic, thermopneumatic, electrostatic, electromagnetic actuation and shape memory alloy (SMA); the most common non-mechanical actuation methods include magneto-hydrodynamic (MHD), electro-hydrodynamic (EHD), and electro-osmotic actuation.

This chapter introduces a novel actuation method applying electrorheological (ER) fluid. The fluid is driven by the drag force induced by particles subject to dipole-dipole interactions in presence of electric field. In addition, this chapter presents a method of evaluating chamber-pump efficiency in terms of motor efficiency and hydraulic efficiency with mechanical check valve and ER valve.

3.2   Chamber Pumps

3.2.1   Design of Screw-Servo Chamber Pump

A chamber pump driven by servo was designed to evaluate the efficiency of it. As shown in Fig. 3-1, a servo motor was employed in the setup, providing torque for the screw via a connector. The plunger, driven by the screw, was designed to exert force on the diaphragm. The deformation of the diaphragm forced liquid out of the chamber. Check valve or ER valve orient the fluid. When the diaphragm deformed back, fluid was sucked in.

(a)   (b)
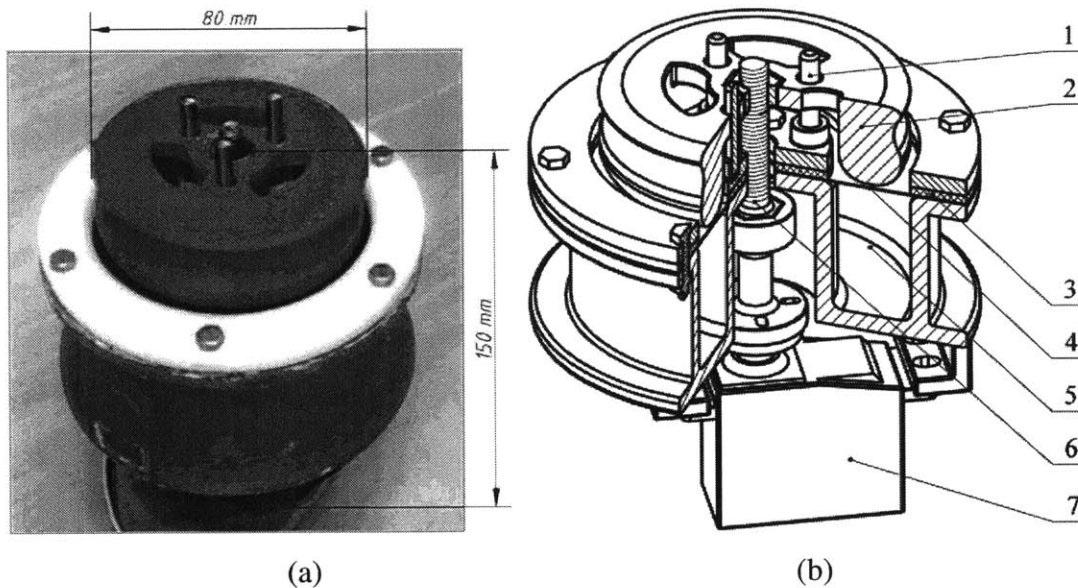
Figure 3-1 (a) A picture of the chamber pump. (b) Sectional view of the 3-D model of the chamber pump with one quarter removed. 1: Guider, 2: Plunger, 3: Gasket, 4: Diaphragm, 5: Chamber, 6: Screw, 7: Servo.

Another similar chamber pump is driven by solenoid. The primary advantage, compared to the servo-driven pump, is the higher frequency achieved by solenoid as shown in Fig. 3-2.
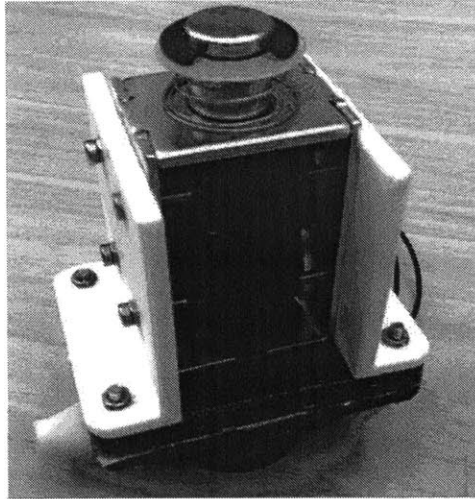
Figure 3-2: A picture of the chamber pump driven by solenoid.

3.2.2 Evaluation of motor performance

To measure the efficiency of the motor, a group of experiments were simply designed by measuring the input power and the output power. The input power is the product of current and voltage from the power supply. The output power was measured by a weight and the distance.

As shown in Fig. 3-2, the power input gets larger when the voltage increases. The first 5 seconds shows the servo motor does negative work, while the last 5 seconds positive. The figure suggests that for voltage above 9.0 volts, the power input fluctuates obviously because the output power nearly exceeds the nominal power. In addition, it can be noticed that an apparent overshoot and instability occur during the transition at about 5 seconds. The Chart 3.1 shows the efficiency which is calculated from the results in the last 5 seconds. It indicates that the efficiency peaks at around 6.0 volts, and then drops dramatically.
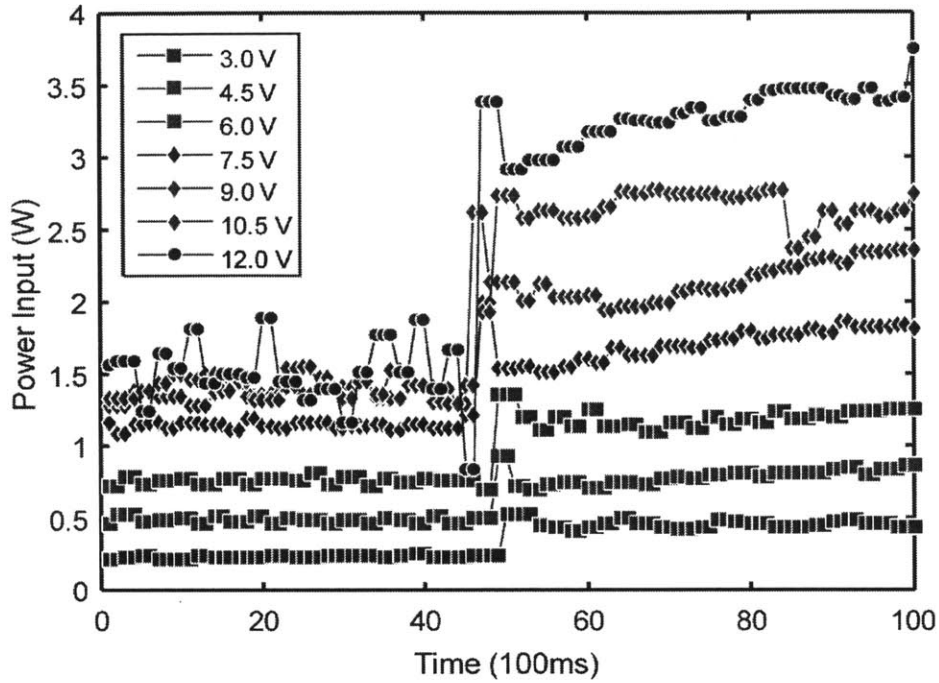
Figure 3-3: Power input versus time. The voltage ranges from 3.0 V to 12.0 V. One cycle of 10 s is shown in the figure.

Chart 3.1: Efficiency of the servo motor. (Voltage U (V) and current I (A) was acquired directly from the power supply. Distance h (m) was defined by the height of the weight, which was lifted by the servo.)

Voltage U (V)	3.0	4.5	6.0	7.5	9.0	10.5	12.0
Current I (A)	0.153	0.173	0.199	0.230	0.234	0.253	0.265
Time t (s)	5	5	5	5	5	5	5
Distance h (m)	0.096	0.174	0.288	0.390	0.438	0.485	0.540
Efficiency mgh/UIt (%)	20.2	21.6	23.3	21.5	20.1	17.7	16.4

3.2.3 Evaluation of hydraulic performance

The hydraulic performance was evaluated by the efficiency of the experimental setup as shown in Fig. 3-4. The input power was provided by Texture Analyzer. The output power was defined as the product of the output pressure and according volume transported. Experiments were conducted using mechanical check valve and electrorheological (ER) valve.
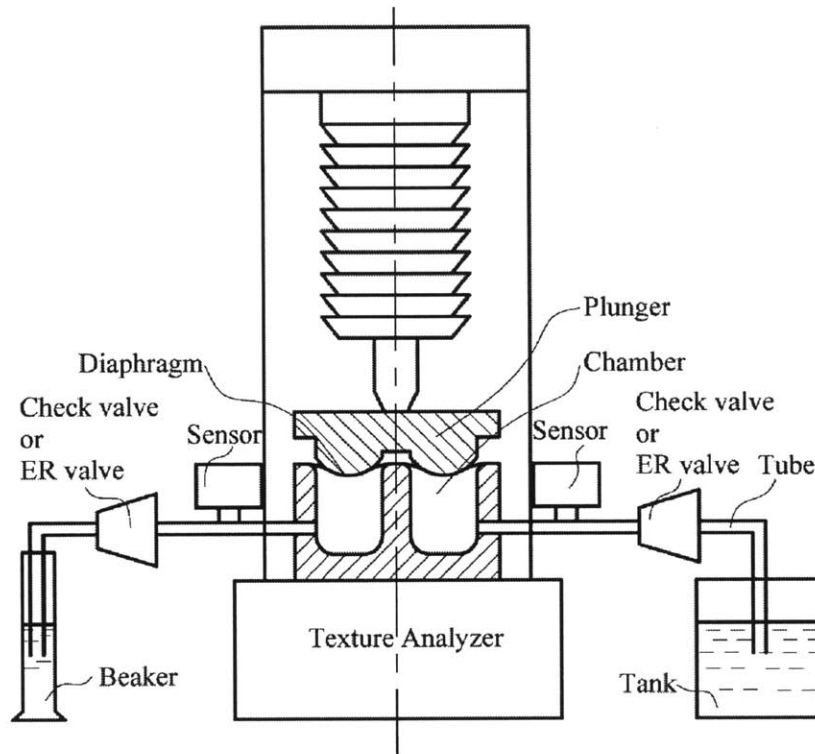
Figure 3-4: Experimental setup for the evaluation of hydraulic performance. Texture Analyzer was implemented to control the distance and velocity of the plunger.

The experimental results of hydraulic efficiency are shown in Fig. 3-5. The overall efficiency is no larger than 10 percent. Generally, as the velocity of the plunger increases, the efficiency experiences an abrupt decrease. The highest efficiency is

achieved under the condition of a plunger distance of 5 mm and a velocity of 2 mm/s.
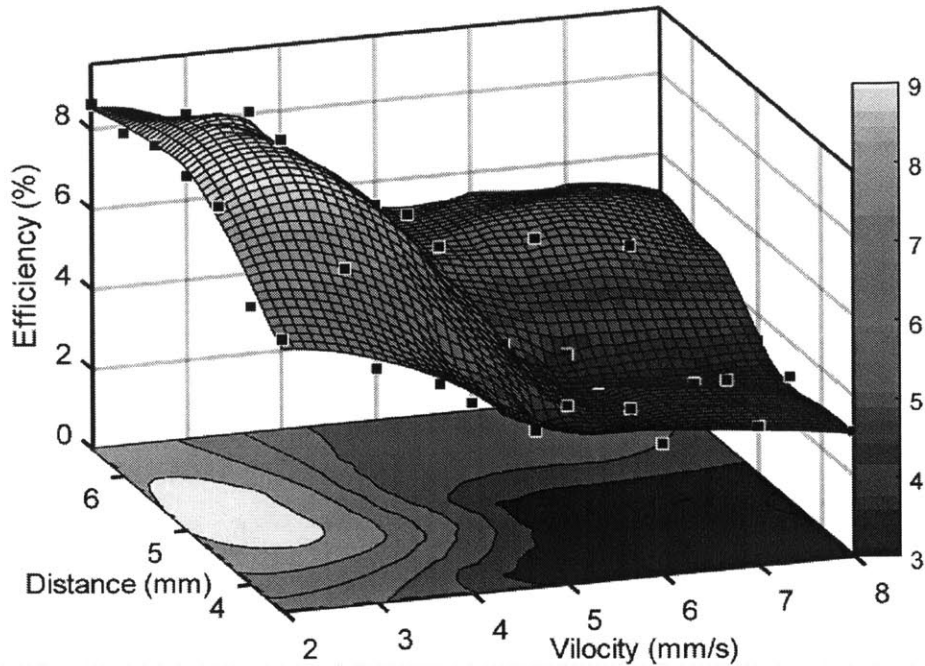
Figure 3-5: Hydraulic efficiency. The distance of plunger exerted on the diaphragm ranges from 2 mm to 8 mm. The velocity indicates the speed of plunger.

3.2.4 Evaluation with Electrorheological Valve

Electrorheological (ER) valve has been widely explored. We applied ER valves in our hydraulic systems to evaluate the effectiveness of ER valve in terms of the average pressure and efficiency. The results are shown in Table 3-2. It suggests a significant improvement in both cases. (In this calculation, the power input for ER valve was not accounted due to the small current, so the real improvement of the efficiency may be below the experimental result.)

Table 3-2: Pressure and efficiency comparison

	Parameter		Efficiency		Improvement (%)
	Velocity (mm/s)	Stoke (mm)	Check Valve	ER Valve	
Average pressure (Psi)	2	4.5	0.093	0.120	29
	3	5	0.092	0.115	25
	4	5.5	0.090	0.112	24
Efficiency (%)	2	4.5	8.86	9.32	5.2
	3	5	8.10	8.75	8.0
	4	5.5	7.28	7.85	7.8

3.3   Solid State pumps

3.3.1   Design of the First prototype

The first prototype of solid state pump was designed by a laser-cut plate sandwiched between another two plates. A picture of the solid state pump is shown in Fig. 3-6. Two tube fittings were designed as inlet and outlet to circulate electrorheological fluids. Electrodes were made of copper printed on flexible plastic paper, which could be wrapped around the channel. Each electrode is labeled in Fig. 3-7, in which eight pairs of positive and negative electrodes are presented. A horizontal electric field is formed within the channel. Due to the layout of electrodes, the electric field gradient within the channel varies.
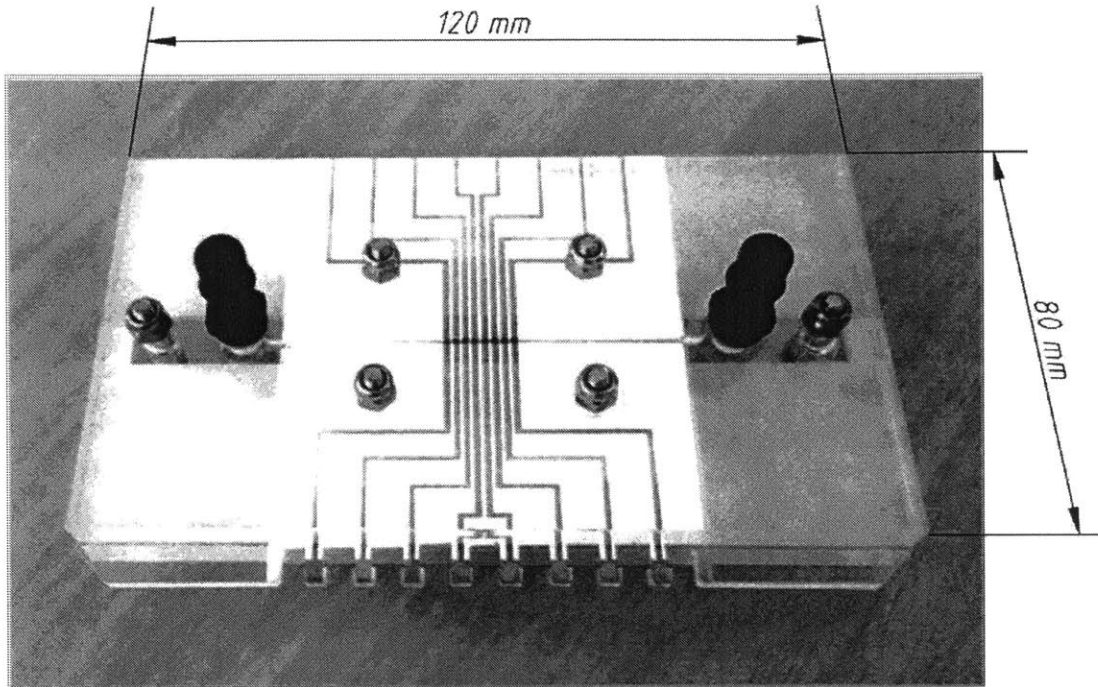
Figure 3-6: A picture of the solid state pump. (Channel width: 0.5 mm, Electrodes width: 0.7 mm, Electrodes spacing: 0.3 mm.)
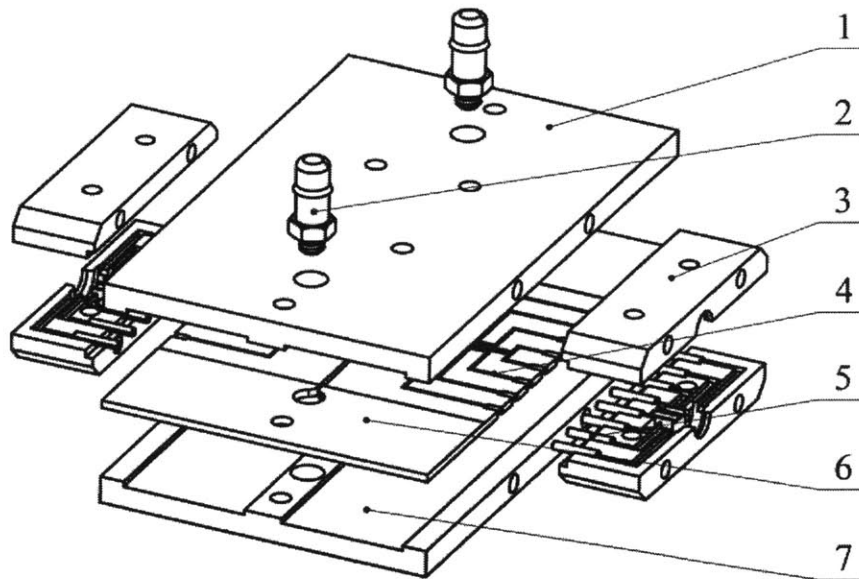
Figure 3-7: Exploded view of the 3-D model of the solid state pump. 1: Upper plate, 2: Tube fitting, 3: Electric connector, 4: Printed circuits, 5: Electrodes, 6: Middle plate, 7: Lower plate.
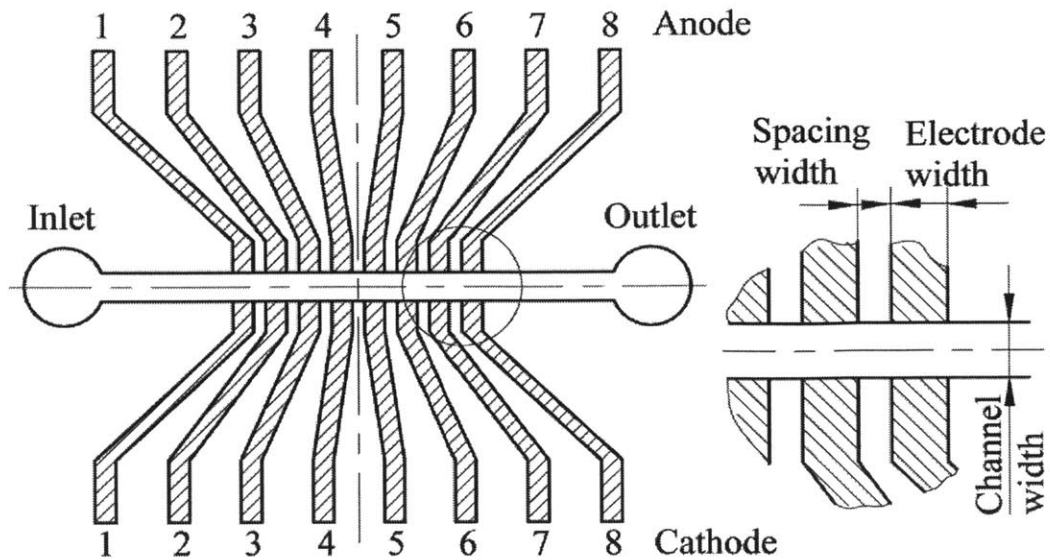
Figure 3-8: A schematic of the channel. Different variables have been explored: electrode width: 0.7 mm, 0.9 mm, 1.2 mm; spacing: 0.5 mm, 0.7 mm, 0.9 mm; channel width: 0.3 mm, 0.5 mm, 0.7 mm. Eight pairs of electrodes, wrapped around the middle plate, are equally distributed along the channel.

An experimental setup was designed to evaluate the performance of the solid state pump. Pressure differential was measured by the height of the liquid surface in the pitot tubes. A picture of the solid state pump with pitot tubes is shown in Fig. 3-9.
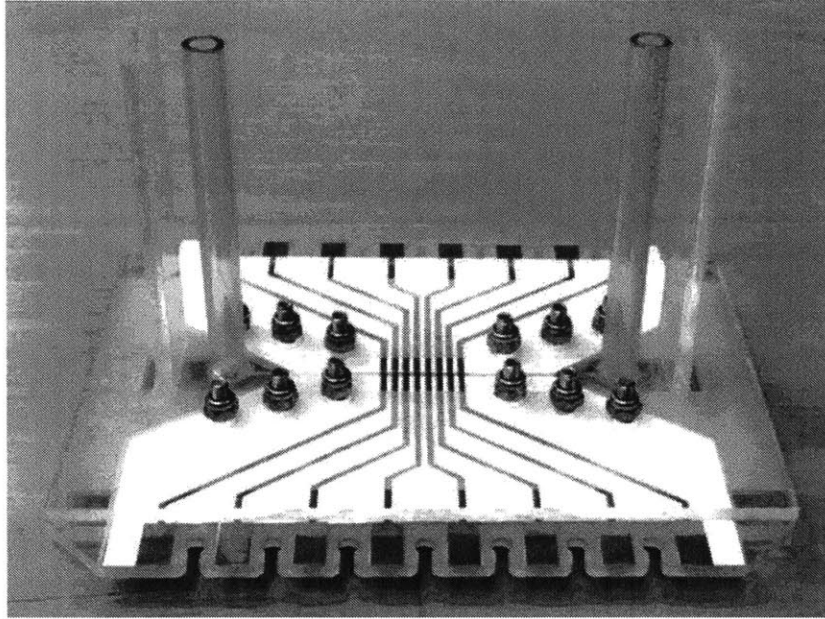
Figure 3-9: A picture of the solid state pump with pitot tubes to evaluate pressure differential. (Channel width: 0.5 mm; Electrodes width: 0.7 mm; Electrodes spacing: 0.3 mm.)

3.3.2 Design of the Second Prototype

A drawback of the first prototype solid state pump is the limited length of the channel. We propose designing a circular channel so that the solid particles could be accelerated. The mobility of the solid particles was evaluated by the second prototype as shown in Fig. 3-10.
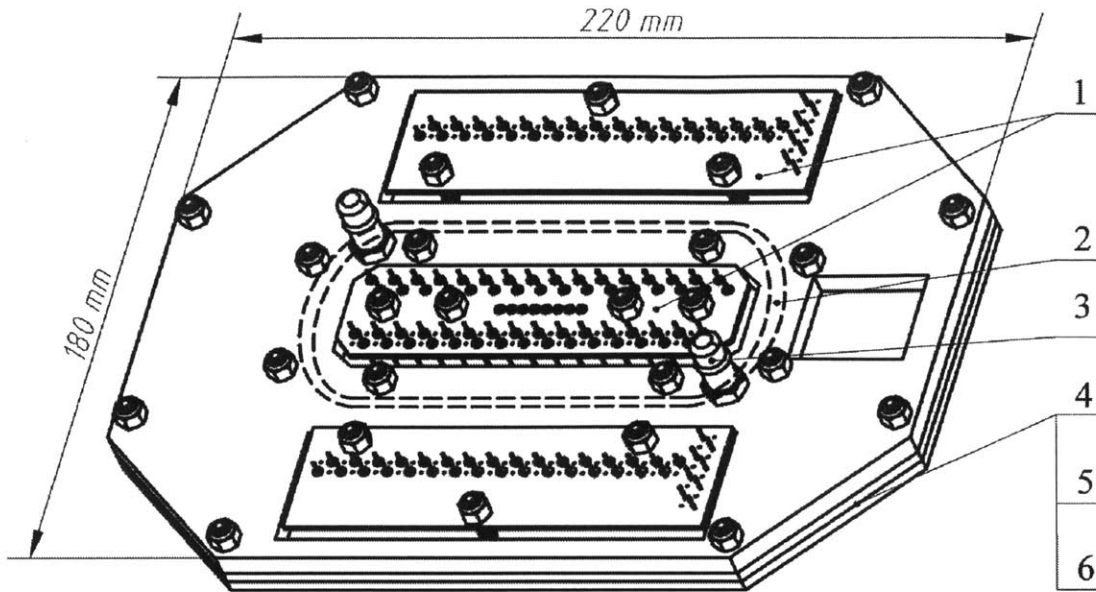
Figure 3-10: 3-D model of the second prototype solid state pump. 1: Printed circuit board, 2: Race-Track channel, 3: Tube fitting, 4: Upper plate, 5: Middle plate (with a circular channel), 6: Lower plate.

3.3.3 Simulation and Experiments

The voltage gradient has been varied. A typical sequence of voltage gradient is shown in Fig. 3-10. The result of the simulation, shown in Fig. 3-11, derives from simple particle-based Stokesian dynamics with periodic boundaries. Particle force results from electric field, dipole-dipole interactions, and drag. Fig. 3-11 suggests that solid particles aggregate in the vicinity of electrodes and the particle density around the electrodes, to some extent, depends on the magnitude of the voltage. When the voltage gradient changes cyclically, the particles are driven along the channel so that flow is induced.
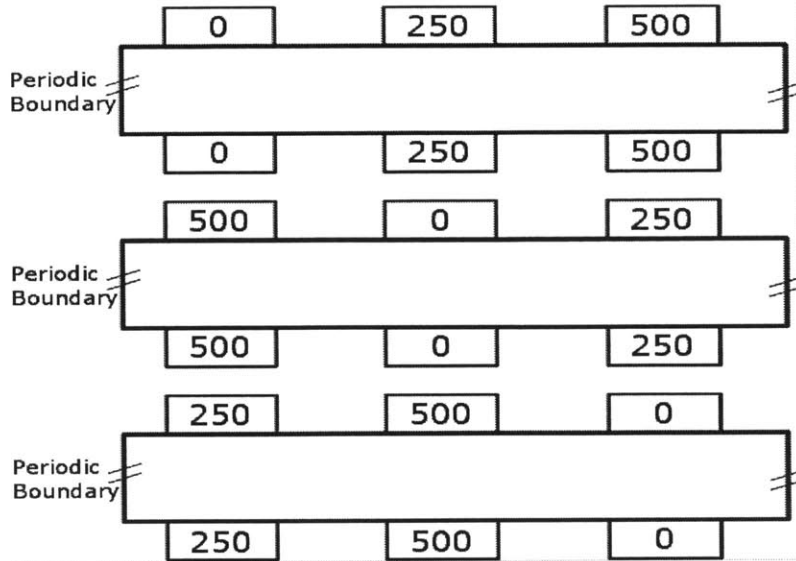
Figure 3-11: A typical voltage gradient. The number indicates the voltage (V) on each electrode. (Image was provided by Matthew Demers.)
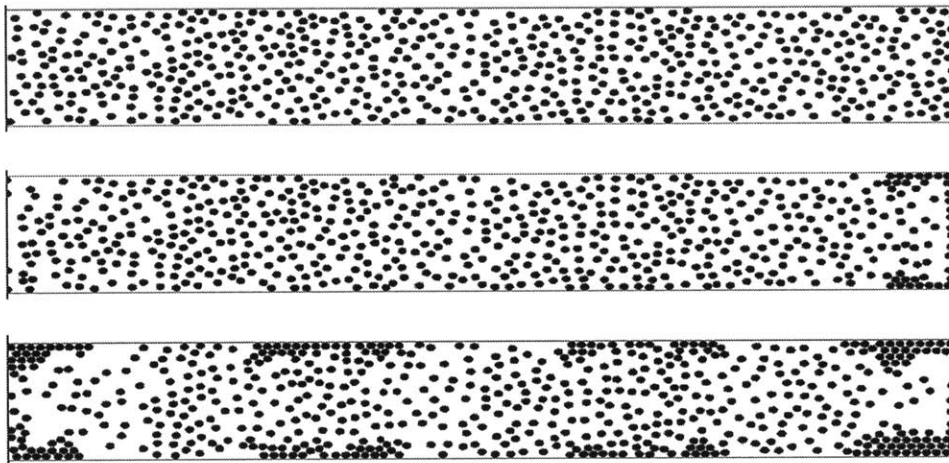
Figure 3-12: Particle aggregation simulation with the channel. The small black dots indicate the dipole particles. (Image was provided by Matthew Demers.)

To verify the simulation model for particle movement, the first prototype solid state pump with pitot tubes was powered by the voltage wave pattern as shown in Fig. 3-12. A microscope was used to observe the particle movement. A sequence of pictures is shown in Fig. 3-13, which is in a good agreement of the simulation results. It could be noticed that as a voltage gradient was applied, an obvious vortex formed

resulting in aggregation of solid particles in the vicinity of electrodes.
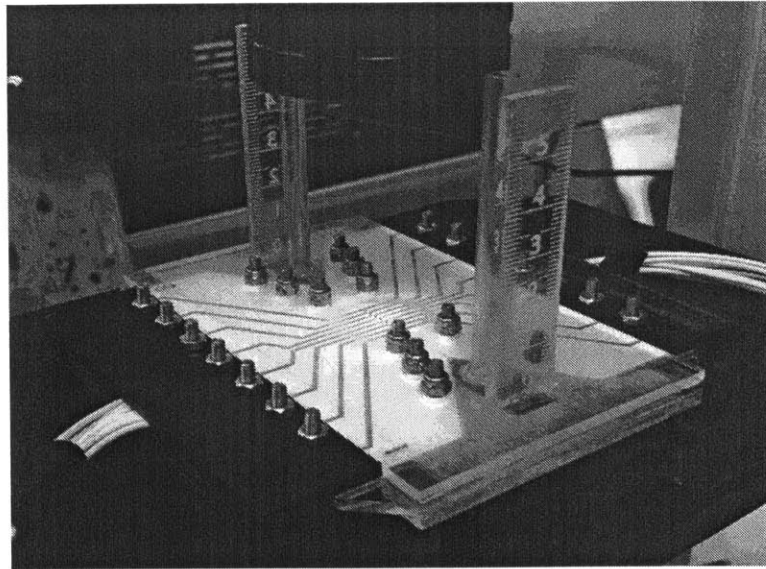
Figure 3-13: Experimental setup to observe solid particle movement in the channel (Image was provided by Michael Evzelman)
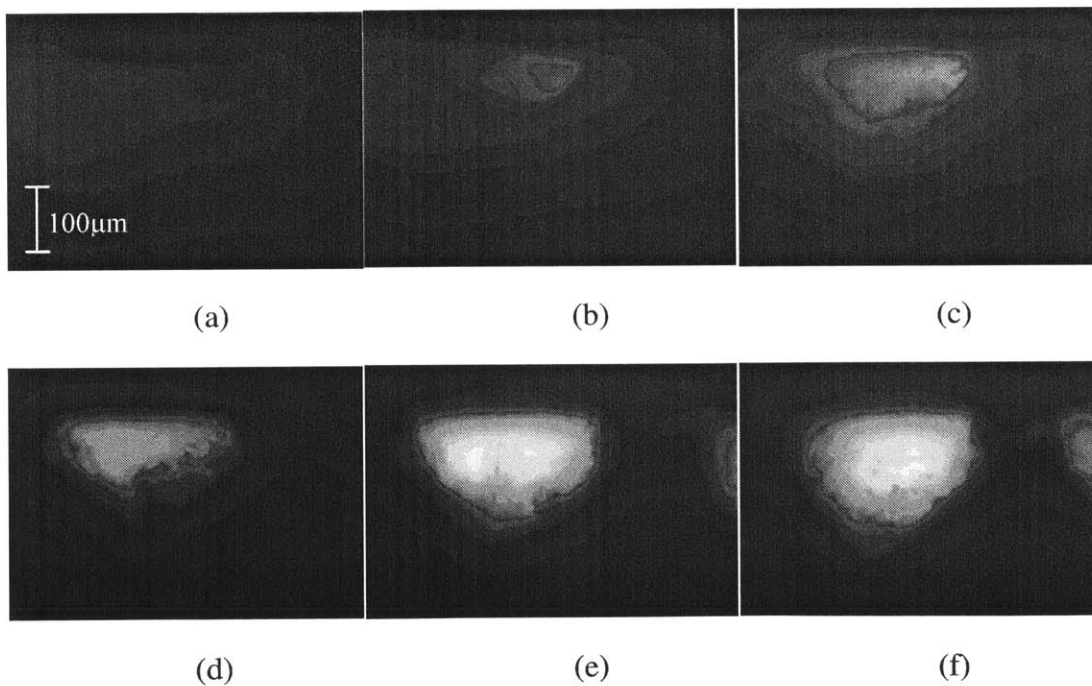
Figure 3-14: A sequence of pictures of the solid particle movement (Provided by Michael Evzelman). From (a) to (f), it shows the particles within the channel at t = 1 s, 6 s, 11 s, 16 s, 21 s, 26 s. (Image was provided by Michael Evzelman.)

Chapter 4

Conclusions and Future work

4.1 Conclusions

The research presented in this thesis is motivated by the inefficiency problem of micropumps and the potential applications for magnetorheological (MR) and electrorheological (ER) fluids.

In Chapter 2, we investigated the sealing method for micro-scale gear pumps. Four simplified mathematical were built for curved channels with a rectangular cross section. The experimental results showed a good conformation with the simplified model. On one hand, to study the static performance, experiments were designed to study the performance with a weak magnetic field. It could be observed that the deformation of the magnetic chains was more evident as flow rates increases and the magnetic chains finally collapse.

On the other hand, experiments were designed to investigate the dynamic sealing performance. As the rotational speed increased, the pressure differential went down abruptly from the static state to the dynamic due to the unequally induced Couette flow rate resulted from the asymmetric magnetic field intensity. The flow is modeled as Darcy flow through porous media for one branch, and as Bingham flow for the other. The flow rate induced by the rotational speed of the disk was reduced by the porous media in the branch exposed in stronger magnetic field. This

asymmetric induced flow rate accounted for the discrepancy of the pressure differential between the static state and the dynamic. However, as the rotational speed increases, the pressure differential remained nearly stable, indicating that the effectiveness of the porous media was restrained, which could be accounted by the excess of the deformation saturation of magnetic brushes.

In Chapter 3, a typical chamber pump driven by servo motor and solenoid were designed. First, the performance of the servo motor was evaluated by measuring the input power and the output power. The experiments showed that, for voltage above 9.0 volts, the power input fluctuated obviously because the output power nearly exceeded the nominal power. In addition, it could be noticed that an apparent overshoot and instability occurred during the transition at about 5 seconds. Second, the hydraulic performance was evaluated by the efficiency of the experimental setup using Texture Analyzer. The experimental results of hydraulic efficiency suggested that the overall efficiency is no larger than 10 percent. Generally, as the velocity of the plunger increases, the efficiency experiences an abrupt decrease. The highest efficiency is achieved under the condition of a plunger distance of 5 mm and a velocity of 2 mm/s. Experiments were conducted using mechanical check valve and electrorheological (ER) valve. A significant improvement could be observed with ER valve.

In addition, two prototypes of micropumps driven by ER fluids were designed and manufactured. The first prototype is designed to drive ER fluids within a straight channel. Parameters are varied and tested by an experimental setup with pitot tubes measuring the pressure differential. The channel of the second prototype is designed to be circular, in which solid particles are accelerated by voltage gradient. The voltage gradient has also been varied. Simulation, derived from simple particle-based Stokesian dynamics with periodic boundaries, was operated. The results show that solid particles aggregate in the vicinity of electrodes and the

particle density around the electrodes, to some extent, depends on the magnitude of the voltage. When the voltage gradient changes cyclically, the particles are driven along the channel so that flow is induced.

4.2 Future work

The methods of dynamic sealing for micro-scale gear pumps and solid state pumps using ER fluids driven by voltage gradient may be applied to other conditions or devices. Further potential applications in other fields may be worthwhile exploring.

For the dynamic sealing of micro-scale gear pumps, there is still large space to be further investigated. In this thesis, the magnetic field from permanent magnet was designed to set the intensity within the channel to be a constant. A variable magnetic field may be interesting to study by a coil, in which an optimal sealing performance might be achieved by controlling the current in the coil.

For the solid state pump driven by ER fluids, the waveform of the voltage needs to be explored further. Right now the magnitude of voltage to drive the ER fluid is set to be around 500 V. To lower this peak magnitude, the waveform and frequency of the voltage may be investigated. Also, an optimized waveform will attribute to achieving the optimal performance or specific pressure differential or flow rate.

Bibliography

[1]   Abhari, F., Jaafar, H., & Yunus, N. A. M. (2012). A comprehensive study of micropumps technologies. Int. J. Electrochem. Sci, 7, 9765-9780.

[2]   Tay, F. E. (Ed.). (2002). Microfluidics and BioMEMS applications (p. 2002). Norwell, MA, USA: Kluwer Academic Publishers.

[3]   Woias, P. (2005). Micropumps—past, progress and future prospects. Sensors and Actuators B: Chemical, 105(1), 28-38.

[4]   Junwu, K., Zhigang, Y., Taijiang, P., Guangming, C., & Boda, W. (2005). Design and test of a high-performance piezoelectric micropump for drug delivery. Sensors and Actuators A: Physical, 121(1), 156-161.

[5]   Cui, Q., Liu, C., & Zha, X. F. (2007). Study on a piezoelectric micropump for the controlled drug delivery system. Microfluidics and Nanofluidics, 3(4), 377-390.

[6]   Van Lintel, H. T. G., Van de Pol, F. C. M., & Bouwstra, S. (1988). A piezoelectric micropump based on micromachining of silicon. Sensors and actuators, 15(2), 153-167.

[7]   Smits, J. G. (1990). Piezoelectric micropump with three valves working peristaltically. Sensors and Actuators A: Physical, 21(1), 203-206.

[8]   Linnemann, R., Woias, P., Senfft, C. D., & Ditterich, J. A. (1998, January). A self-priming and bubble-tolerant piezoelectric silicon micropump for liquids and gases. In Micro Electro Mechanical Systems, 1998. MEMS 98. Proceedings., The Eleventh Annual International Workshop on (pp. 532-537). IEEE.

[9]   Van de Pol, F. C. M., Van Lintel, H. T. G., Elwenspoek, M., & Fluitman, J. H. J. (1990). A thermopneumatic micropump based on micro-engineering techniques.Sensors and Actuators A: Physical, 21(1), 198-202.

[10]   Jeong, O. C., & Yang, S. S. (2000). Fabrication and test of a thermopneumatic micropump with a corrugated p+ diaphragm. Sensors and Actuators A: Physical, 83(1), 249-255.

[11]   Cooney, C. G., & Towe, B. C. (2004). A thermopneumatic dispensing micropump. Sensors and Actuators A: Physical, 116(3), 519-524.

[12]   Benard, W. L., Kahn, H., Heuer, A. H., & Huff, M. A. (1998). Thin-film shape-memory alloy actuated micropumps. Microelectromechanical Systems, Journal of, 7(2), 245-251.

[13]   Benard, W. L., Kahn, H., Heuer, A. H., & Huff, M. A. (1997, June). A titanium-nickel shape-memory alloy actuated micropump. In Solid State Sensors and Actuators, 1997. TRANSDUCERS'97 Chicago., 1997 International Conference on (Vol. 1, pp. 361-364). IEEE.

[14] Makino, E., Mitsuya, T., & Shibata, T. (2001). Fabrication of TiNi shape memory micropump. Sensors and Actuators A: Physical, 88(3), 256-262.

[15] Sim, W. Y., Yoon, H. J., Jeong, O. C., & Yang, S. S. (2003). A phase-change type micropump with aluminum flap valves. Journal of Micromechanics and Microengineering, 13(2), 286.

[16] Kim, K. H., Yoon, H. J., Jeong, O. C., & Yang, S. S. (2005). Fabrication and test of a micro electromagnetic actuator. Sensors and Actuators A: Physical,117(1), 8-16.

[17] Yun, K. S., Cho, I. J., Bu, J. U., Kim, C. J., & Yoon, E. (2002). A surface-tension driven micropump for low-voltage and low-power operations.Microelectromechanical Systems, Journal of, 11(5), 454-461.

[18] Richter, A., Plettner, A., Hofmann, K. A., & Sandmaier, H. (1991). A micromachined electrohydrodynamic (EHD) pump. Sensors and Actuators A: Physical, 29(2), 159-168.

[19] Tsai, J. H., & Lin, L. (2002). A thermal-bubble-actuated micronozzle-diffuser pump. Microelectromechanical Systems, Journal of, 11(6), 665-671.

[20] Kargov, A., Werner, T., Pylatiuk, C., & Schulz, S. (2008). Development of a miniaturised hydraulic actuation system for artificial hands. Sensors and Actuators A: Physical, 141(2), 548-557.

[21] Yang, X., Grosjean, C., & Tai, Y. C. (1999). Design, fabrication, and testing of micromachined silicone rubber membrane valves. Microelectromechanical Systems, Journal of, 8(4), 393-402.

[22] Rapp, R., Schomburg, W. K., Maas, D., Schulz, J., & Stark, W. (1994). LIGA micropump for gases and liquids. Sensors and Actuators A: Physical, 40(1), 57-61.

[23] Van de Pol, F. C. M., Van Lintel, H. T. G., Elwenspoek, M., & Fluitman, J. H. J. (1990). A thermopneumatic micropump based on micro-engineering techniques.Sensors and Actuators A: Physical, 21(1), 198-202.

[24] Zengerle, R., Ulrich, J., Kluge, S., Richter, M., & Richter, A. (1995). A bidirectional silicon micropump. Sensors and Actuators A: Physical, 50(1), 81-86.

[25] Shen, M., Yamahata, C., & Gijs, M. A. M. (2008). A high-performance compact electromagnetic actuator for a PMMA ball-valve micropump. Journal of Micromechanics and Microengineering, 18(2), 025031.

[26] Yao, S., Hertzog, D. E., Zeng, S., Mikkelsen, J. C., & Santiago, J. G. (2003). Porous glass electroosmotic pumps: design and experiments. Journal of Colloid and Interface Science, 268(1), 143-153.

[27] Reichmuth, D. S., Chirica, G. S., & Kirby, B. J. (2003). Increasing the performance of high-pressure, high-efficiency electrokinetic micropumps using zwitterionic solute additives. Sensors and Actuators B: Chemical, 92(1), 37-43.

[28] Conrad, H., & Sprecher, A. F. (1991). Characteristics and mechanisms of electrorheological fluids. Journal of statistical physics, 64(5-6), 1073-1091.

[29] Block, H., Kelly, J. P., Qin, A., & Watson, T. (1990). Materials and mechanisms in electrorheology. Langmuir, 6(1), 6-14.

[30] Yoshida, K., Kikuchi, M., Park, J. H., & Yokota, S. (2002). Fabrication of micro electro-rheological valves (ER valves) by micromachining and experiments.Sensors and Actuators A: Physical, 95(2), 227-233.

[31] Choi, S. B., Cho, M. S., & Wereley, N. M. (2006). Wheel-slip control of a passenger vehicle using an electrorheological valve pressure modulator.Proceedings of the Institution of Mechanical Engineers, Part D: Journal of Automobile Engineering, 220(5), 519-529.

[32] Ulrich, S., Böhme, G., & Bruns, R. (2009, February). Measuring the response time and static rheological properties of electrorheological fluids with regard to the design of valves and their controllers. In Journal of Physics: Conference Series (Vol. 149, No. 1, p. 012031). IOP Publishing.

[33] Whittle, M., Atkin, R. J., & Bullough, W. A. (1995). Fluid dynamic limitations on the performance of an electrorheological clutch. Journal of Non-Newtonian Fluid Mechanics, 57(1), 61-81.

[34] Choi, S. B., & Lee, D. Y. (2005). Rotational motion control of a washing machine using electrorheological clutches and brakes. Proceedings of the Institution of Mechanical Engineers, Part C: Journal of Mechanical Engineering Science, 219(7), 627-637.

[35] Wereley, N. M., Lindler, J., Rosenfeld, N., & Choi, Y. T. (2004). Biviscous damping behavior in electrorheological shock absorbers. Smart Materials and Structures, 13(4), 743.

[36] Lindler, J. E., & Wereley, N. M. (1999). Double adjustable shock absorbers using electrorheological fluid. Journal of intelligent material systems and structures, 10(8), 652-657.

[37] Williams, E. W., Rigby, S. G., Sproston, J. L., & Stanway, R. (1993). Electrorheological fluids applied to an automotive engine mount. Journal of Non-Newtonian Fluid Mechanics, 47, 221-238.

[38] Sproston, J. L., Stanway, R., Williams, E. W., & Rigby, S. (1994). The electrorheological automotive engine mount. Journal of Electrostatics, 32(3), 253-259.

[39] Stanway, R., Sproston, J. L., Prendergast, M. J., Case, J. R., & Wilne, C. E. (1992). ER fluids in the squeeze-flow mode: an application to vibration isolation.Journal of electrostatics, 28(1), 89-94.

[40] Williams, E. W., Rigby, S. G., Sproston, J. L., & Stanway, R. (1993). Electrorheological fluids applied to an automotive engine mount. Journal of Non-Newtonian Fluid Mechanics, 47, 221-238.

[41] Bonnecaze, R. T., & Brady, J. F. (1992). Dynamic simulation of an electrorheological fluid. The Journal of chemical physics, 96(3), 2183-2202.

[42] Martin, J. E., Odinek, J., Halsey, T. C., & Kamien, R. (1998). Structure and dynamics of electrorheological fluids. Physical Review E, 57(1), 756.

[43] Furusho, J., Sakaguchi, M., Takesue, N., & Koyanagi, K. I. (2002). Development of ER brake and its application to passive force display. Journal of Intelligent Material Systems and Structures, 13(7-8), 425-429.

[44] Sakaguchi, M., Furusho, J., & Takesue, N. (2001, March). Passive force display using ER brakes and its control experiments. In Virtual Reality, 2001. Proceedings. IEEE (pp. 7-12). IEEE.

[45] Hill, J. C., & Van Steenkiste, T. H. (1991). Response times of electrorheological fluids. Journal of applied physics, 70(3), 1207-1211.

[46] Ginder, J. M., Davis, L. C., & Elie, L. D. (1996). Rheology of magnetorheological fluids: Models and measurements. International Journal of Modern Physics B,10(23n24), 3293-3303.

[47] Goncalves, F. D., Koo, J. H., & Ahmadian, M. (2006). A review of the state of the art in magnetorheological fluid technologies-Part I: MR fluid and MR fluid models. The Shock and Vibration Digest, 38(3), 203-219.

[48] Tao, R., & Jiang, Q. (1998). Structural transitions of an electrorheological and magnetorheological fluid. Physical Review E, 57(5), 5761.

[49] Jolly, M. R., Bender, J. W., & Carlson, J. D. (1998, June). Properties and applications of commercial magnetorheological fluids. In 5th Annual International Symposium on Smart Structures and Materials (pp. 262-275). International Society for Optics and Photonics.

[50] Rabinow, J. (1948). The magnetic fluid clutch. American Institute of Electrical Engineers, Transactions of the, 67(2), 1308-1315.

[51] Kwok, N. M., Ha, Q. P., Nguyen, M. T., Li, J., & Samali, B. (2007). Bouc–Wen model parameter identification for a MR fluid damper using computationally efficient GA. ISA transactions, 46(2), 167-179.

[52] Lee, H. S., & Choi, S. B. (2000). Control and response characteristics of a magneto-rheological fluid damper for passenger vehicles. Journal of Intelligent Material Systems and Structures, 11(1), 80-87.

[53] Kim, K., & Jeon, D. (1999). Vibration suppression in an MR fluid damper suspension system. Journal of Intelligent Material Systems and Structures,10(10), 779-786.

[54] Sassi, S., Cherif, K., Mezghani, L., Thomas, M., & Kotrane, A. (2005). An innovative magnetorheological damper for automotive suspension: from design to experimental characterization. Smart Materials and Structures, 14(4), 811.

[55] YOKOTA, S., YOSHIDA, K., & KONDOH, Y. (1999). A pressure control valve using MR fluid. In Proceedings of the JFPS International Symposium on Fluid Power (Vol. 1999, No. 4, pp. 377-380).

[56] Yoo, J. H., & Wereley, N. M. (2002). Design of a high-efficiency magnetorheological valve. Journal of Intelligent Material Systems and Structures, 13(10), 679-685.

[57] Guo, N. Q., Du, H., & Li, W. H. (2003). Finite element analysis and simulation evaluation of a magnetorheological valve. The international journal of advanced manufacturing technology, 21(6), 438-445.